Available online at www.sciencedirect.com

SCIENCE DIRECT®

Tectonophysics 421 (2006) 269–297

TECTONOPHYSICS

www.elsevier.com/locate/tecto

^{40}Ar/^{39}Ar thermochronology of the Kampa Dome, southern Tibet: Implications for tectonic evolution of the North Himalayan gneiss domes

Mark Quigley [a,*], Yu Liangjun [b], Liu Xiaohan [b], Christopher J.L. Wilson [a], Mike Sandiford [a], David Phillips [a]

[a] School of Earth Sciences, The University of Melbourne, Victoria, 3010, Australia
[b] Institute of Geology and Geophysics, Chinese Academy of Sciences, Beijing 100029, China

Received 23 January 2006; received in revised form 30 April 2006; accepted 1 May 2006
Available online 30 June 2006

Abstract

Structural and thermochronological studies of the Kampa Dome provide constraints on timing and mechanisms of gneiss dome formation in southern Tibet. The core of Kampa Dome contains the Kampa Granite, a Cambrian orthogneiss that was deformed under high temperature (sub-solidus) conditions during Himalayan orogenesis. The Kampa Granite is intruded by syn-tectonic leucogranite dikes and sills of probable Oligocene to Miocene age. Overlying Paleozoic to Mesozoic metasedimentary rocks decrease in peak metamorphic grade from kyanite+staurolite grade at the base of the sequence to unmetamorphosed at the top. The Kampa Shear Zone traverses the Kampa Granite — metasediment contact and contains evidence for high-temperature to low-temperature ductile deformation and brittle faulting. The shear zone is interpreted to represent an exhumed portion of the South Tibetan Detachment System. Biotite and muscovite ^{40}Ar/^{39}Ar thermochronology from the metasedimentary sequence yields disturbed spectra with 14.22±0.18 to 15.54±0.39 Ma cooling ages and concordant spectra with 14.64±0.15 to 14.68±0.07 Ma cooling ages. Petrographic investigations suggest disturbed samples are associated with excess argon, intracrystalline deformation, mineral and fluid inclusions and/or chloritization that led to variations in argon systematics. We conclude that the entire metasedimentary sequence cooled rapidly through mica closure temperatures at ~14.6 Ma. The Kampa Granite yields the youngest biotite ^{40}Ar/^{39}Ar ages of ~13.7 Ma immediately below the granite–metasediment contact. We suggest that this age variation reflects either varying mica closure temperatures, re-heating of the Kampa Granite biotites above closure temperatures between 14.6 Ma and 13.7 Ma, or juxtaposition of rocks with different thermal histories. Our data do not corroborate the "inverse" mica cooling gradient observed in adjacent North Himalayan gneiss domes. Instead, we infer that mica cooling occurred in response to exhumation and conduction related to top-to-north normal faulting in the overlying sequence, top-to-south thrusting at depth, and coeval surface denudation.

Keywords: Tibet; Himalaya; Gneiss domes; ^{40}Ar/^{39}Ar thermochronology

1. Introduction

The North Himalaya gneiss domes (NHGD) (Fig. 1) have emerged as key features of the Himalayan–Tibetan

---

* Corresponding author. Tel.: +61 3 8344 4996; fax: +61 3 8344 7761.
E-mail address: m.quigley2@pgrad.unimelb.edu.au (M. Quigley).

0040-1951/$ - see front matter © 2006 Elsevier B.V. All rights reserved.
doi:10.1016/j.tecto.2006.05.002

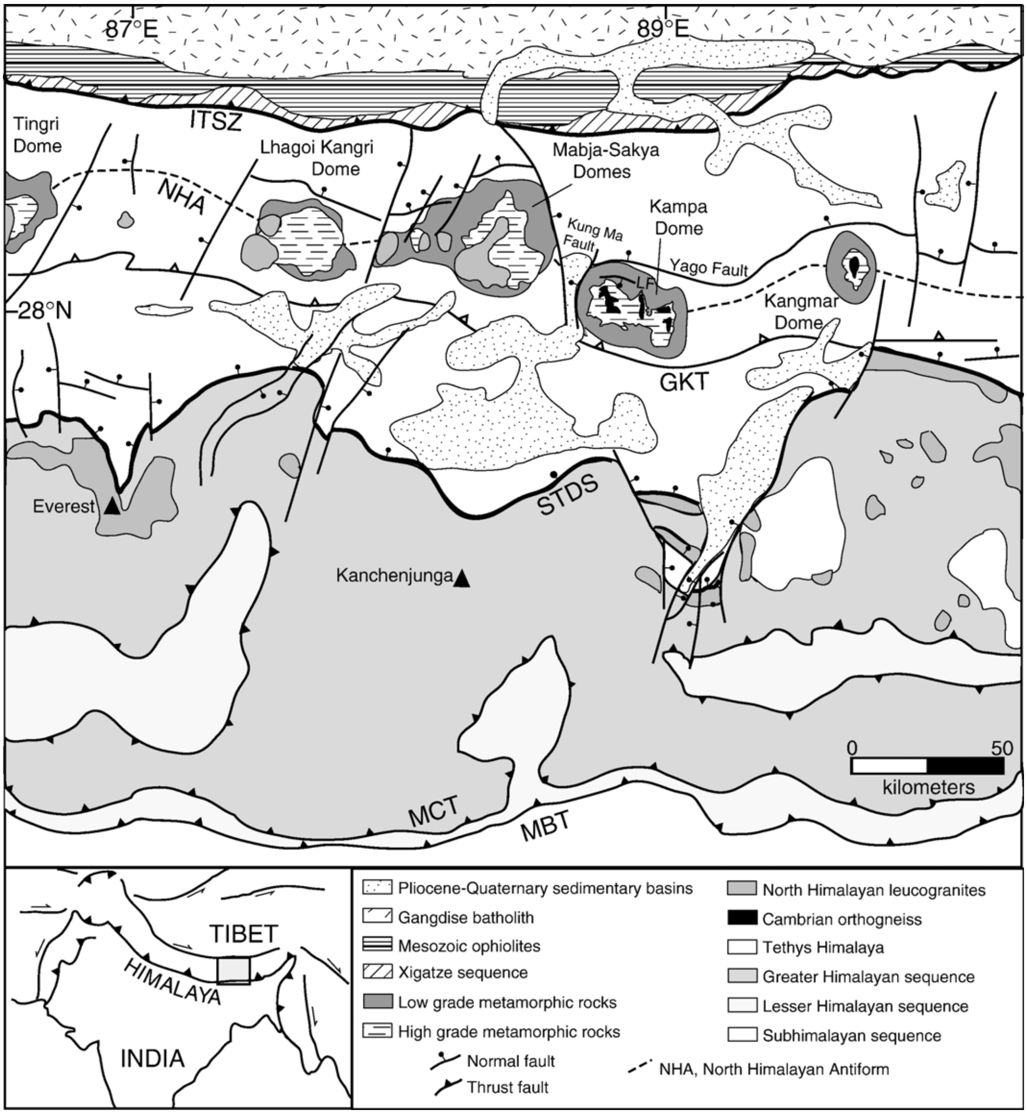

Fig. 1. Regional tectonic map of the central Himalayan orogen including the North Himalayan gneiss domes, modified from Burchfiel et al. (1992), Burg (1983), Watts and Harris (2005), and Zengqian et al. (1986). MBT, Main Boundary Thrust; MCT, Main Central Thrust; STDS, South Tibetan Detachment System; GKT, Gyirong–Kangmar Thrust; ITSZ, Indus–Tsangpo Suture Zone. Inset, modified from Burchfiel et al. (1992) and Tapponnier et al. (1982), shows location of regional map.

orogen because they expose middle crustal rocks that were deformed, metamorphosed and melted during the India–Asia collision (Burg et al., 1984; Debon et al., 1986; Lee et al., 2000, 2004, in press; Zhang et al., 2004; Aoya et al., 2005, in press). The origin of gneiss domes is highly debated both in the Himalayan–Tibetan orogen and worldwide (Eskola, 1949; Burg et al., 1984; Le Fort, 1986; Le Fort et al., 1987; Chen et al., 1990; Lee et al., 2000, 2004, in press; Whitney et al., 2004 and references therein). Recent insights into the processes of gneiss dome formation in the North Himalaya have been achieved through the coupling of structural, stratigraphic and metamorphic studies with $^{40}Ar/^{39}Ar$ thermochronology (e.g., Lee et al., 2000, in press).

The Kampa Dome (Quigley et al., 2004) forms one of a series of NHGD that collectively define the east–west trending North Himalayan Antiform, between the Indus–Tsangpo Suture Zone to the north and the South Tibetan Detachment System to the south (Fig. 1). The Indus–Tsangpo Suture Zone marks the lithotectonic boundary between accreted crustal blocks of Asian affinity to the north and rocks of Indian affinity to the south (Burg and Chen, 1984). The South Tibetan Detachment System is a major north-dipping normal fault zone that juxtaposes low-metamorphic grade to unmetamorphosed hangingwall rocks of the Tethyan Himalaya to the north with high grade Greater Himalayan sequence rocks to the south (Burchfiel et al., 1992). Shear zones exhumed within the cores of the NHGD have been proposed to represent deeper crustal level exposures of the South Tibetan Detachment System (Chen et al., 1990; Hauck et al., 1998; Lee et al., 2000, in press).

The Kampa Dome is located between the well-studied Kangmar Dome to the east (Burg and Chen, 1984; Chen et al., 1990; Lee et al., 2000) and Mabja–Sakya Domes to the west (Lee et al., 2004, in press; Zhang et al., 2004) (Fig. 1). The Kangmar and Mabja–Sakya Domes display evidence for similar structural and metamorphic histories (Lee et al., 2000, in press), involving: (1) initial ~N–S contraction and crustal thickening; (2) peak metamorphism and ~N–S oriented high-strain horizontal extension and vertical thinning; and (3) subsequent development of domal geometries at mid-crustal depths of 10–20 km (Lee et al., 2000). Most of the NGHD lie in the hangingwall of the N-dipping Gyirong–Kangmar Thrust (Fig. 1), which places fossiliferous Jurassic rocks on top of fossiliferous Cretaceous rocks with an estimated vertical throw of ~2000 m (J.P. Burg, personal commun.). The domal geometries associated with the NHGD have been ascribed to thrusting along this system (Burg et al., 1984; Hauck et al., 1998; Lee et al., 2000, in press). This hypothesis was founded largely on the observation that mica ^{40}Ar/^{39}Ar cooling ages increase with structural depth in the Mabja–Sakya and Kangmar Domes, which Lee et al. (2000, in press) attributed to refrigeration of the base of the section during underthrusting of cold Tethyan sediments. Alternatively, Le Fort (1986) and Le Fort et al. (1987) proposed that the NHGD formed as a result of diapiric rise of buoyant melts. Chen et al. (1990) concluded that the Kangmar Dome formed during crustal extension related to the gravitational collapse of the Himalayan topographic front, and suggested that the NHGD share common characteristics with metamorphic core complexes of the United States of America. The thermal–mechanical models of Beaumont et al. (2004) predicted crustal doming due to (1) efficient mid-crustal channel flow into localized destabilized zones of horizontally extended and vertically thinning crust, and/or (2) squeezing and upward insertion of mid-crust into overlying upper crust during thrusting over a frontal ramp (i.e. the Gyirong–Kangmar Thrust). Lee et al. (2004, in press) suggested that the domal geometry in Mabja–Sakya Dome resulted from a combination of contractional, extensional, and diapiric mechanisms.

These studies inferred that the mechanisms that formed the NHGD were regional in extent. Although the NHGD are strikingly similar along strike there appear to be differences between domes including (1) the petrography and distribution of rock types composing the domal cores, and to some extent, the metasedimentary carapace, (2) the distribution of low-grade metamorphism, (3) the nature and kinematics of the contact zone between the core of the domes and the overlying carapace, and (4) the spatial distribution of ^{40}Ar/^{39}Ar mica ages. Each of these characteristics may have significant implications for the processes which led to formation of the NHGD.

In this paper, we provide new geologic mapping, stratigraphy, petrography and ^{40}Ar/^{39}Ar thermochronology from the previously unstudied Kampa Dome. In addition, we summarize the results of Quigley et al. (in review) who conducted detailed structural and U–Pb geochronological studies of the dome. We aim to evaluate the similarities and differences between Kampa Dome and the adjacent NHGD, provide a mechanism for doming in light of this data, and thereby assess whether dome-forming processes were indeed regional in extent. Our results suggest that the Kampa Dome formed in response to coeval upper-crustal extension and contraction at depth and that ^{40}Ar/^{39}Ar cooling ages record mid-Miocene, top-down conductive cooling instead of the inverted thermal profile observed in adjacent domes (Lee et al., 2000, in press).

2. Geologic setting of the North Himalayan gneiss domes

The NHGD outcrop within the Tethyan Himalaya; a sedimentary sequence deposited on the northern continental margin of India over the Cambrian to Eocene interval (Gansser, 1964; Le Fort, 1975; Yin et al., 1988; Gaetani and Garzanti, 1991; Hodges, 2000). The cores of many of the NHGD contain granitic orthogneiss that was strongly deformed during the Himalayan orogeny (Burg et al., 1984; Debon et al., 1986; Chen et al., 1990; Lee et al., 2000). Orthogneiss from Kangmar Dome (Kangmar Granite) yields Cambrian U–Pb zircon ages of 562±4 Ma (Scharer et al., 1986) to 508±1 Ma (Lee et al., 2000). The Kangmar Granite is interpreted to form the Indian basement upon which the Tethyan sequence was deposited (Burg et al., 1984; Zhang et al., 1986; Lee et al., 2000). However, Aoya et al. (2005) obtained U–Pb SHRIMP zircon rim ages of 18.5 to 17.2 Ma from orthogneiss in the Malsahan Dome and suggested that the Malashan Granite intruded into and metamorphosed the Tethyan sequence during the Miocene. Petrologic descriptions, trace element geochemistry and Sr-isotope data (Zhang et al., 2004) suggest that the NHGD orthogneisses may be lithologically equivalent to the upper part of the Greater Himalayan sequence (i.e. High Himalayan Crystalline Series), structurally beneath the STDS (Fig. 1). High-strain zones developed along the contact between the orthogneiss and Tethyan sequence in the NHGD have been interpreted as exhumed portions of the STDS (Chen et al., 1990; Hauck et al., 1998; Lee et al., 2000, 2004, in press).

The metasedimentary rocks immediately overlying the orthogneiss are generally accepted to be Carboniferous (Chen et al., 1990) to Permian (Brookfield, 1993) in age, based on scarcely observed fossiliferous assemblages. These rocks are overlain by a >4 km thick section of Mesozoic marine clastic sediments, interpreted to record a near-continuous period of deposition on the northern India passive margin subsequent to Gondawana breakup (Brookfield, 1993). Deposition of this sequence appears to have continued until the latest Cretaceous to Eocene, when the collision between India and Asia began to influence depositional conditions (Willems et al., 1996).

Many of the NHGD have been intruded by a series of leucocratic granite bodies (Debon et al., 1986; Watts and Harris, 2005). Textural relationships within the Mabja–Sakya Domes established that leucogranite plutonism was both synchronous with and postdated the late stages of development of a subhorizontal foliation attributed to crustal extension (Lee et al., 2004, in press). U–Pb dating of accessory phases indicates that leucogranite magmatism in Mabja–Sakya Dome occurred from ~27.5 Ma to ~10 Ma (Scharer et al., 1986; Zhang et al., 2004; Lee et al., in press). Lee et al. (in press) obtained U/Pb zircon and monazite ages of ~14.2 to 14.5 Ma from undeformed leucogranites in Mabja–Sakya Dome and inferred that ductile deformation had ceased by this time.

3. Geology of Kampa Dome

Early geologic maps of southern Tibet depicted the Kampa Dome (then un-named) as two doubly plunging sub-domes cored by granitic orthogneiss and flanked by Paleozoic sedimentary rocks (Burg, 1983). A major north-striking normal fault system (Kung Ma Fault) and Quaternary basin (Kung Ma Basin) was recognized in the western dome (Figs. 1 and 2). A series of north-dipping reverse faults composing the Gyirong–Kangmar Thrust (Burg and Chen, 1984; Ratschbacher et al., 1994) were identified to the south (Figs. 1 and 2). Subsequent regional geologic maps produced by Zengqian et al. (1986) indicated that Kampa Dome was composed of a single, east–west trending elliptical Cambro–Ordovician undifferentiated gneissic core (including a small body of undifferentiated granite gneiss) overlain by concentric outcrop patterns of Cambrian through to Triassic strata. Faults were inferred to offset sedimentary rocks to the immediate north (Yago Fault, Fig. 1), east (Kung Ma Fault), and west of the dome. Quigley et al. (2004) discovered a major shear zone at the core-cover contact and mapped small leucogranite bodies in the core of the dome. Watts and Harris (2005) produced geologic maps of the NHGD including Kampa Dome from ASTER data, which they used to distinguish leucogranites and older, biotite-rich orthogneiss in the cores of the domes. The leucogranite bodies described by Quigley et al. (2004) were not identified by Watts and Harris (2005) because many of these intrusions are smaller than the 15 to 90 m/pixel ASTER resolution.

Geologic mapping of Kampa Dome was conducted using 15 m/pixel scale ASTER satellite images as base maps and aided by the use of high-resolution SPOT image of the Kampa Dome region. Field observations and remote mapping indicate that the Kampa Dome is composed of a series of three sub-domes (Fig. 2a) cored by granitic orthogneiss and leucogranite intrusions and overlain by a carapace of metamorphosed to unmetamorphosed sedimentary rocks.

3.1. Lithostratigraphy

The Kampa Granite exposed in the core of Kampa Dome (Fig. 4a) is composed of quartz (~40%), microcline–orthoclase (~30%) twinned oligoclase

Fig. 2. Geologic maps and images of the Kampa Dome. (a) Generalized geological sketch map of Kampa Dome and major structural elements, from field mapping and remote sensing, modified from Burg (1983) and Zengqian et al. (1986). The dome is composed of three subdomes cored by the Kampa Granite. The inferred eastern subdome is exposed in two segments due to erosion. The dome resides in the hangingwall of the Gyirong–Kangmar Thrust (Gyirong–Kangmar Thrust). (b) ASTER satellite image of the central part of the western subdome, showing clearly visible geologic contacts between the Kampa Granite orthogneiss (ogn), overlying pelitic schist (ps) and lower marble units (mar) in the bottom right, and upper marble, quartzite, and phyllite (phy) and slate units in the top left. ASTER images were used to trace geologic contacts into inaccessible parts of Kampa Dome. (c) Geologic map of the western Kampa Dome. Location of map shown by dashed line in (a). Location of (b) shown by dashed box in (c). Geologic contacts based on field mapping or inferred from ASTER imagery. Structural measurements indicate gentle doming of the S_2 exhumational foliation and associated lineation outward from the Kampa Granite core. The contact between the Kampa Granite and overlying pelite is marked by the Kampa Shear Zone. Locations of $^{40}Ar/^{39}Ar$ thermochronology samples shown.

(25%) and biotite (3–5%) with minor amounts of muscovite±epidote±clinozosite±titanite±zircon (<2%). Quartz grains display well developed undulatory extinction, are ribboned and contain serrated, irregular grain boundaries. Microcline–orthoclase is perthitic and myremekitic, locally sericitized, and coarse-grained

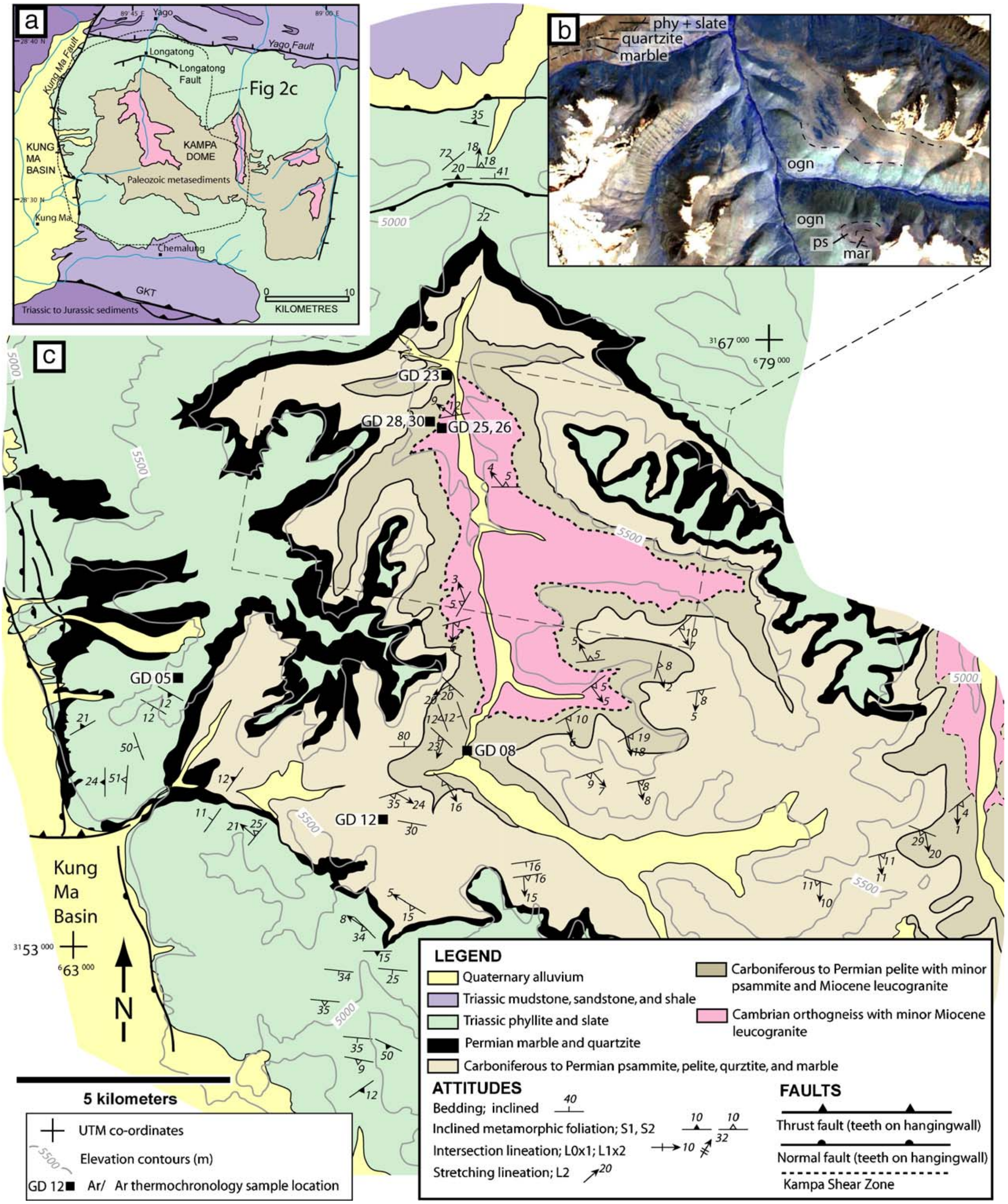

(>3 mm), defining an augen gneissic texture. Clusters of strongly aligned biotite crystals with undulatory extinction and grain sizes ranging from 0.3 to 1.2 mm define a gently dipping foliation in the Kampa Granite. The granite contains high-temperature microstructures within the foliation that indicate a mixture of coaxial strain, top-to-N shearing and top-to-S shearing. Steeper, lower-temperature (brittle–ductile) top-to-S microstructures are locally developed on the S limb of Kampa Dome where they cross-cut the high-temperature foliation.

Quigley et al. (in review) obtained two dominant ^{206}Pb/^{238}U SHRIMP (sensitive, high resolution ion microprobe) zircon age populations of 506 ± 3 Ma and 527 ± 6 Ma from the Kampa Granite and inferred that the granite is a Cambrian intrusion. However, a strongly deformed and altered metasedimentary xenolith was observed within the Kampa Granite near the contact with overlying metasedimentary rocks. Quigley et al. (in review) suggested that the xenolith was derived from the overlying metasedimentary sequence and incorporated into the Kampa Granite during high-temperature (sub-solidus) Himalayan deformation.

Sedimentary rocks overlying the Kampa Granite range from upper amphibolite facies at the base of the section to unmetamorphosed at the top (Fig. 3). We estimated a total thickness of ~3300 m for the metasedimentary sequence. The basal ~800 m include interlayered pelite, psammite, quartzite, and marble.

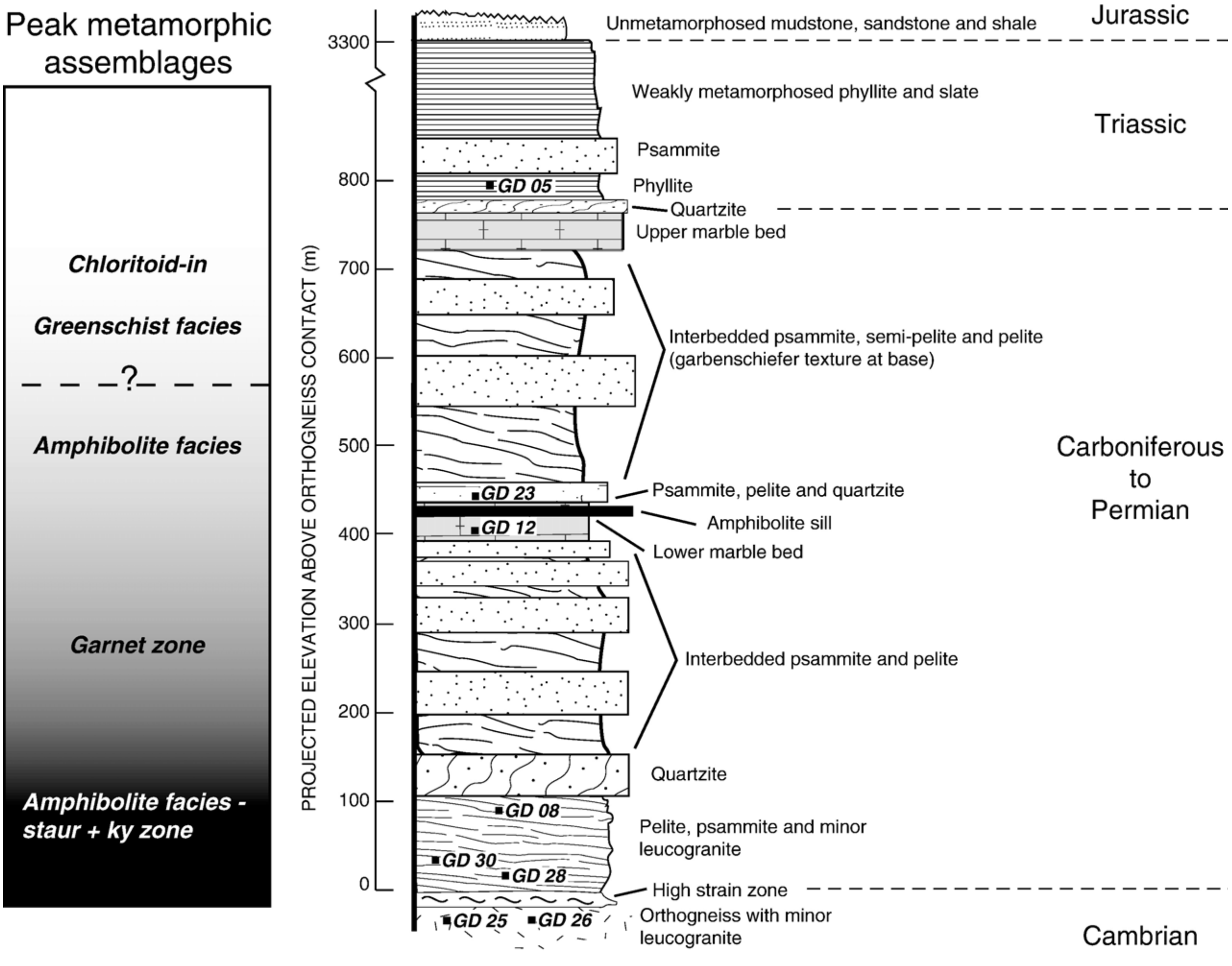

Fig. 3. Stratigraphic section of Kampa Dome showing major stratigraphic units, documented changes in peak metamorphic mineral assemblage, inferred ages and age-boundaries of strata, and stratigraphic positions of ^{40}Ar/^{39}Ar thermochronology samples. Stratigraphic thicknesses estimated by projecting flanking stratigraphy into a vertical column overlying the Kampa Granite core.

Pelitic rocks include the assemblage quartz (15–30%), muscovite (15–40%), biotite (15–20%), plagioclase (10%), K-feldspar (0–5%) staurolite (0–5%), garnet (0–5%), kyanite (0–5%), chlorite (0–5%), ilmenite (0–5%) and tourmaline (0–2%) with accessory titanite. Interlayered psammitic rocks generally contain relatively higher proportions of quartz, feldspar and biotite with lesser amounts of muscovite and garnet, and locally

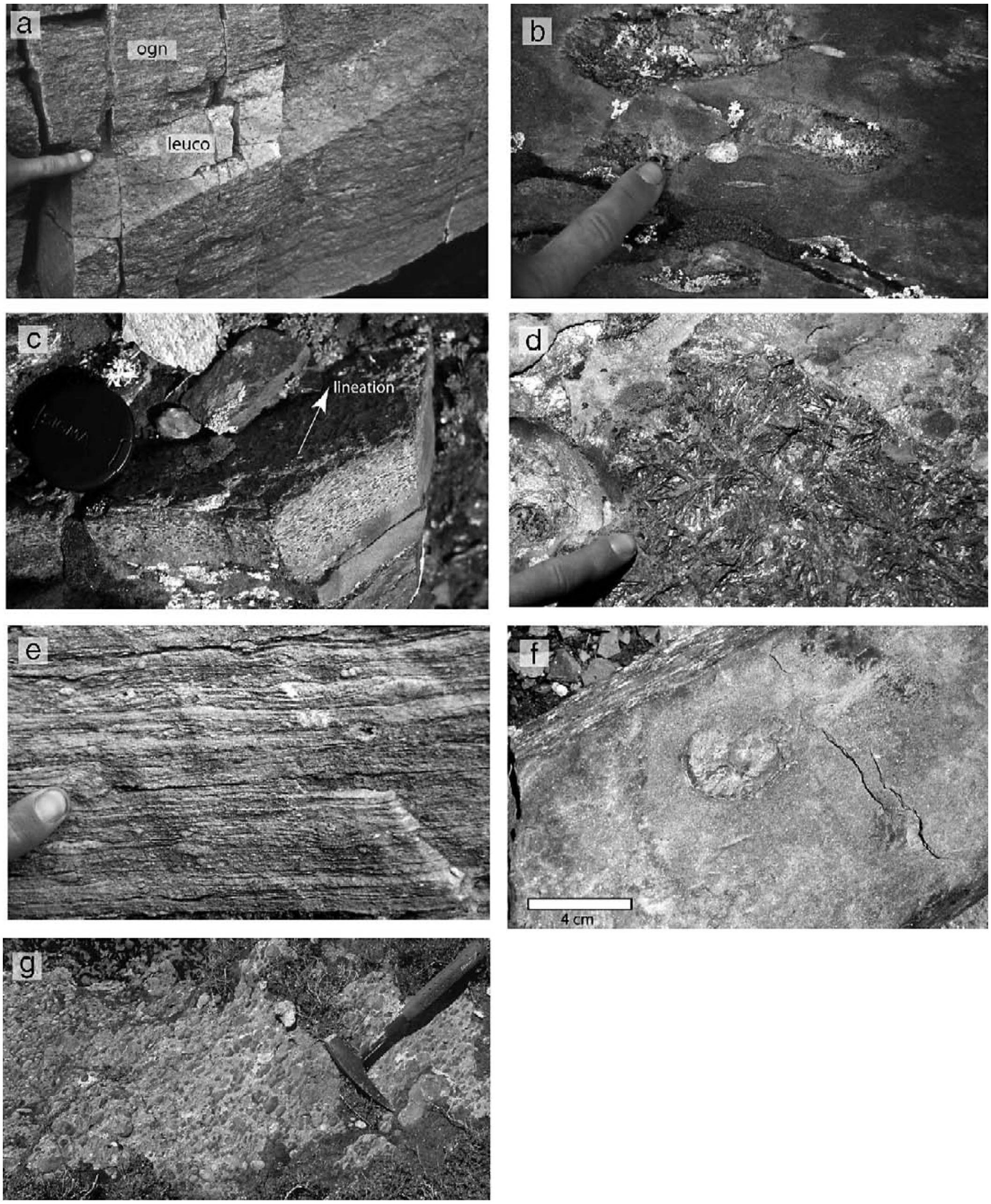

Fig. 4. Field photographs of prominent lithologic and textural features of Kampa Dome. (a) Strongly foliated Kampa Granite (ogn) intruded by thin, garnet-bearing leucogranite sill (leuco). The sill cross-cuts the Kampa Granite foliation at a low angle but contains a mildly developed internal foliation, implying syn-kinematic emplacement. (b) Rounded granite pebble in psammite. Presence of the pebble indicates that granite terrains were aerially exposed during deposition of the psammite, although the provenance of the pebble is unknown. (c) Lineated coarse-grained amphiboles in psammite. (d) Coarse-grained radiating kyanite bundles along the contact of quartzite and pelite in lower parts of the metasedimentary sequence. (e) Deformed crinoids in strongly foliated marble unit (at finger tip and elsewhere). (f) Small ammonite fossil in phyllite unit. (g) Conglomeritic bed in phyllite unit.

contain significant (up to 5%) concentrations of fine-grained disseminated graphite. The psammitic beds are locally conglomeritic, containing small, rounded clasts of granite (Fig. 4b) and quartzite. Granite clasts are unfoliated but lithologically similar to the Kampa Granite, consistent with our interpretation that the granite formed the basement to the sedimentary sequence prior to Himalayan deformation. A finer-grained unit composed of thin (5–10 cm thick), lightly coloured quartz + feldspar beds contains radiating and locally lineated bundles of amphibole (Fig. 4c). Contacts between interbedded pelites and pale-coloured quartzites locally contain large radiating bundles of kyanite (Fig. 4d). Foliation–textural relationships indicate that amphibole and kyanite overgrow a penetrative foliation but are also wrapped by the foliation and locally rotated parallel to a stretching lineation, indicating late syn-tectonic growth.

Marbles (Fig. 4e) are principally composed of calcite + dolomite (95%) with varying amounts of quartz, phlogopite, and muscovite, and local concentrations of clinozoisite, tremolite, diopside, and hematite within thin (1–2 cm) darker coloured beds. Strongly deformed crinoid fossils are common (Fig. 4e).

The lower-grade metasedimentary rocks overlying the upper marble unit are composed of dark green to black-coloured, fine-grained pelitic slate and phyllite with minor amounts of weakly metamorphosed siltstone and sandstone. Pelites contain the assemblage biotite (30–40%), quartz (30–40%), muscovite (20%) and graphite (5–10%) with large (>3 mm) chloritoid porphyoblasts (3–5%), minor amounts of garnet at the deeper structural levels, and minor amounts of tourmaline. On the south side of the dome, small (~4 cm diameter) goniatite fossils with rounded zigzag sutures are contained within thin (<1 m thick) conglomeritic beds, indicating a Devonian–Carboniferous depositional age (Fig. 4f). The slate and phyllite grade upwards into a sequence of pyrite-bearing siltstone and sandstone, gray-weathering limestone, and darkly coloured shale. We did not examine these units in detail, however Burg (1983) and Zengqian et al. (1986) assigned them a Jurassic age.

3.2. Intrusive rocks

The Kampa Granite and overlying metasedimentary rocks are intruded by a series of leucogranite dikes and sills ranging in thickness from ~10 to 200 cm. The leucogranite suite includes medium-grained, pegmatitic, and aplitic varieties. The intrusions are generally equivalent in their compositions, containing quartz (~30%), microcline (~30%), oligoclase (~30%), biotite (~5%), muscovite (3–5%) and garnet (1–2%) with trace amounts of epidote ± tourmaline ± zircon. All of the leucogranite bodies observed in the Kampa Dome are deformed. Leucogranite sills are both concordant and discordant with respect to the strong foliation in the Kampa Granite, however they contain an internal foliation parallel to the gneissic foliation, indicating that they intruded during development of the foliation (Fig. 4a).

Quigley et al. (in review) obtained $^{206}Pb/^{238}U$ SHRIMP ages of 504–547 Ma from cores and rims of euhedral igneous-type zircons from two leucogranite intrusions. Discordant age populations of 491–259 Ma and 53–32 Ma were obtained from anhedral-to-subhedral metamict zircons. Given that the Kampa leucogranites must clearly post-date the Carboniferous rocks that they intrude, the zircons must be xenocrysts. Age constraints may be obtained by comparing the Kampa leucogranites to dated, lithologically and texturally equivalent leucogranite intrusions from the adjacent Mabja–Sakya Dome. Zhang et al. (2004) obtained a U–Pb age of ~27.5 Ma from a deformed, garnet-bearing leucogranite pluton that appears to be the lithological equivalent of the leucogranite sills in the Kampa Dome. A deformed, late syn-tectonic, two-mica leucogranite pegmatite dike yielded a $^{206}Pb/^{238}U$ age of 23.1 ± 0.8 Ma (Lee et al., in press). Similar pegmatite dikes cross-cut leucogranite sills in the Kampa Dome (Quigley et al., in review). Undeformed granites in the Mabja–Sakya Dome yield U–Pb ages of ~14.0–14.6 Ma (Zhang et al., 2004; Lee et al., in press). Providing deformation was roughly synchronous throughout the NHGD, we therefore constrain the age of the Kampa leucogranite suite from ~27.5 Ma to ~14.6 Ma.

Dark-colored, penetratively deformed, 20 to 150 cm thick amphibolite sills containing the assemblage hornblende + plagioclase + epidote ± quartz ± biotite ± garnet are conformably interlayered within the high-grade metasedimentary sequence. The edges of the sills are locally fine-grained implying rapid cooling (chill-margins) and upper and lower contacts with the sedimentary rocks are sharp. The age of these intrusions is unknown.

4. Principal structural elements

4.1. Pre-doming structures

Detailed descriptions of the geometry, style, and kinematics of structures in the Kampa Dome are provided by Quigley et al. (in review). We summarize their results below and in Table 1. Two penetrative, high-temperature deformation events (D_1 and D_2) were identified in Kampa Dome. D_1 structures are best exposed in the Jurassic and upper parts of the Triassic sequence on the N limb of Kampa Dome, where they consist of map-to-mesoscopic scale, upright to gently inclined, open to tight, typically disharmonic F_1 folds. At increasing structural depth in the Triassic unit, F_1 folds acquire a strongly developed, gently N-dipping S_1 axial planar fabric and associated E–W trending, subhorizontal bedding–S_1 intersection lineation. S_1 is defined by aligned micas, graphite, and fine-grained chloritoid at these levels and becomes coarser and more phyllitic with increasing depth towards the top of the Paleozoic sequence.

S_2 originates in middle parts of the Triassic sequence as a gently dipping spaced cleavage that overprints S_1. At increasing structural depth, S_2 increases in intensity and is strongly developed as a penetrative axial planar cleavage to isoclinal F_2 folds of bedding and S_1. In the Paleozoic sequence, bedding and S_1 are transposed parallel to S_2 and F_2 folds are recumbent and isoclinal. S_2 dips to the N on the N limb of the dome, to the S on the S limb of the dome, and is associated with a ~N–S oriented L_2 stretching lineation. Microstructural relations between metamorphic porphyroblasts and foliations in the Paleozoic schist units indicate that staurolite, kyanite, garnet, and chloritoid growth was syntectonic with D_2 deformation (Quigley et al., in review). D_2 succeeded porphyroblast growth, forming symmetric and asymmetric strain shadows on porphyroblasts and locally rotating porphyroblasts into parallelism with L_2.

Rocks at the base of the metasedimentary sequence and underlying Kampa Granite are strongly foliated to mylonitic and collectively compose the Kampa Shear Zone. Shear sense indicators imply predominately top-to-N shearing on both limbs of the dome. Localized top-to-S shear sense indicators associated with quartz veins in the S_1+S_2 composite foliation are crosscut by a leucogranite sill that has been deformed by top-to-N deformation, implying a change in shearing polarity prior to or during leucogranite emplacement. Quigley et al. (in review) interpreted the Kampa Shear Zone to have originated as a top-to-S D_1 high strain zone that changed to a top-to-N shear zone during D_2. Since S_1, S_2, and the Kampa Shear Zone are domed, the formation of Kampa Dome must post-date the formation of these elements. Undeformed granites from the Mabja–Sakya Dome indicate D_2 deformation had ceased by ~14.0 to 14.6 Ma, providing a maximum age for the timing of doming along strike of the Kampa Dome.

4.2. Syn-doming structures

S_2 foliations are offset by thinly spaced (1–10 cm) D_3 shear bands and normal faults in the Kampa Granite that dip more steeply than S_2 and indicate top-to-N movement on the N limb of the dome and top-to-S movement on the S limb of the dome. Shear bands are locally associated with retrograde chlorite and epidote and pseudotachylyte implying deformation under greenschist facies to brittle conditions. These structures record the initiation of doming because they are the first structures to indicate a dome-outward sense of shear. The Kampa Shear Zone also contains greenschist facies metamorphism and brittle faulting suggesting it may have incurred continued movement during doming.

A series of ~E–W striking, 30–50° N-dipping, top-to-N high strain zones of ~0.3 to 500 cm thickness are situated at ~40–100 m spaced intervals throughout the Triassic sequence on the N limb of the dome. These D_3 deformation zones overprint S_1 and S_2 and exhibit evidence for both greenschist facies shearing and brittle deformation. F_3 crenulations of S_1+S_2 with locally developed S_3 axial planes have developed within some

Table 1
Principal structural elements of the Kampa Dome

Foliation/fault group	Element type	Dominant orientation	Kinematic interpretation
Early foliation (S_1)	Metamorphic foliation/cleavage	Steep to moderately N and S dipping	~N–S shortening and crustal thickening
Second foliation (S_2)	Metamorphic foliation and high-strain zones	Shallow dips outward from domal core	N–S extension and exhumation
E–W striking normal faults	Brittle–ductile faults and crenulations	Moderately N or S dipping	N–S extension
E–W striking reverse faults	Brittle faults	Moderately S dipping	N–S contraction
N–S striking normal faults	Brittle faults	Steeply W or E dipping	E–W extension

of these zones. The similar deformational conditions and kinematics associated with D_3 structures suggest that progressive deformation from ductile to brittle conditions synchronous with doming.

D_4 structures include all brittle faults observed in Kampa Dome. E–W striking, steeply to moderately N and S-dipping normal faults such as the Yago and Longatong Faults have estimated offsets of ≥100 m. These faults are truncated by the N–S striking, steeply W-dipping Kung Ma normal fault that traverses the western edge of the Kampa Dome. The Kung Ma Fault truncates glacially-carved valleys and appears to be associated with soft-sediment deformation of Late Pleistocene lacustrine sediment in the adjacent Kung Ma Basin, indicating Quaternary displacement (Quigley, 2006). The largest estimated displacements along the fault occur where it intersects the E–W trending topographic hinge of the Kampa Dome, implying that doming may have continued into the Quaternary. The Kung Ma Fault is offset by a ~WNW striking, gently ENE dipping reverse fault that displaces hillslope colluvium in the SW corner of Kampa Dome (Quigley, 2006). This fault may be a smaller, more modern equivalent of the Gyirong–Kangmar Thrust to the south.

5. ^{40}Ar/^{39}Ar thermochronology

^{40}Ar/^{39}Ar muscovite and biotite thermochronology was used to characterize the cooling history of the Kampa Granite and overlying metasedimentary rocks in Kampa Dome. For the discussions that follow, we used closure temperature estimates of 370±50 °C for muscovite (Lister and Baldwin, 1996; Hames and Bowring, 1994) and 335±50 °C for biotite (Harrison et al., 1985; Grove and Harrison, 1996). Closure temperatures may be affected by variations in mineral composition (Harrison et al., 1985; Grove, 1993), grain size (Hess et al., 1993; Kelley, 1988; Markley et al., 2002), inclusions (Rama et al., 1965), retrogression (Di Vincenzo et al., 2003), and deformation/recrystallization (Kramar et al., 2001; Mulch et al., 2002).

5.1. Previous thermochronology from the NHGD

No prior thermochronologic studies have been conducted in the Kampa Dome, however a large dataset exists for the adjacent domes. Conventional K–Ar and ^{40}Ar/^{39}Ar ages for biotite and muscovite obtained from orthogneiss in the core of Kangmar Dome range from ~13 to 20 Ma (Debon et al., 1986; Maluski et al., 1988; Lee et al., in press). Muscovite ^{40}Ar/^{39}Ar ages are commonly younger than co-existing biotite ^{40}Ar/^{39}Ar ages determined from disturbed spectra (Maluski et al., 1988; Lee et al., 2000), suggesting either non-systematic biotite behavior or muscovite closure at temperatures below the closure temperatures for biotite.

Muscovite and biotite ^{40}Ar/^{39}Ar ages obtained from the overlying metasedimentary sequence at Kangmar range from ~11 to 15 Ma and are younger than those obtained from the orthogneiss (Maluski et al., 1988; Lee et al., 2000). Lee et al. (2000) obtained muscovite ^{40}Ar/^{39}Ar ages generally older than co-existing biotite and noted that mica ages increased with increasing structural depth. The observation that argon ages decreased down structural section was used to support a thrust fault model for gneiss dome formation (Lee et al., 2000, in press).

A wealth of ^{40}Ar/^{39}Ar thermochronologic data has also been collected from the Mabja–Sakya Dome. Zhang et al. (2004) obtained ^{40}Ar/^{39}Ar spot analysis ages of 12 to 10 Ma from micas in the leucogranites coring the dome and Lee et al. (in press) obtained a similar range of ^{40}Ar/^{39}Ar inverse isochron biotite (~12.8 to 13.6 Ma) and muscovite (~13.1 to 13.5 Ma) ages from these leucogranites. Muscovite ages from the overlying metasedimentary rocks increase down structural section from ~12.8 Ma at the top of garnet zone rocks to ~17.1 Ma at the bottom of the garnet zone rocks, consistent with interpretations of the Kangmar Dome data. However, in contrast to Kangmar, muscovite ages then decrease with increasing depth to ~13.4 Ma within staurolite and sillimanite zone rocks and leucogranites. Biotites appear to show a similar pattern and yield ages older than co-existing muscovite at deep structural levels.

5.2. Samples

Eight samples were selected for ^{40}Ar/^{39}Ar thermochronology, from which seven biotite and five muscovite separates were analyzed (Fig. 3, Table 2). Two biotite-bearing samples (GD 25, 26) were collected from the Kampa Granite. Three co-existing biotite+ muscovite samples (GD 08, GD 28, GD 30) were collected from high-grade pelitic schists immediately overlying the Kampa Granite. One muscovite sample was collected from a marble bed (GD12) and one biotite+ muscovite sample was collected from semi-pelitic schist (GD 23) at intermediate crustal levels. A final biotite-bearing sample was collected from Triassic phyllite at the highest crustal level (GD 05). Sample locations appear in Figs. 2 and 3 and ^{40}Ar/^{39}Ar age spectrum are displayed with corresponding projected stratigraphic position in Fig. 6.

Table 2
Petrographic descriptions of micas from Kampa Dome

Sample	Elevation (m)	Mineral	Rocktype	Grain size observed (μm)	Grain size analyzed (μm)	PL color	Retrogression/ alteration	Inclusions [a]	Structure
GD05	5617.5	bt	Slate	100–200 and <50 [b]	150–75	Reddish brown	Chlorite interlayering (?)	Qtz+ilm+gr and fluid inclusions	Strong undulatory extinction, highly internally deformed
GDO8b	5096	bt	Pelite	1000–2000	500–354	Greenish brown	Major Fe-rich chloritization within grains and at grain boundaries	Minor tur+ zrn+ilm	Low internal strain, defines strong foliation
GD08m	5096	musc	Pelite	1000–2000	500–354	Colourless	None observed	None observed	Thin interlayered biotite (minor), defines strong foliation
GD12	5391.2	musc	Marble	300–750 and <75 [b]	500–150	Colourless	Minor hematization on grain boundaries	Minor hem	Inclusion-riddled fibrous muscovite mats locally present
GD23b	4810	bt	Semi-pelite	750–1250	500–354	Dark brown	None observed	Minor zrn+ tur+il	Internally unstrained, define strong foliation
GD23m	4810	musc	Semi-pelite	700–1550	500–354	Colourless	None observed	Minor fluid inclusions	Tightly intergrown muscovite mats with nterlayered biotite
GD25	5030.2	bt	ogn	300–1250	500–354	Dark greenish brown	None observed	Rare zrn	Internally unstrained, defines foliation
GD26	5030.2	bt	ogn	250–750	500–250	Greenish brown	None observed	Rare zrn	Internally unstrained, defines foliation
GD28b	5077.5	bt	Pelite	750–2250	500–354	Reddish brown	Minor chloritization on grain boundaries	Rare zrn	Internally unstrained, defines strong foliation
GD28m	5077.5	musc	Pelite	250–1250	500–354	Colourless	None observed	None observed	Thin interlayered biotite (minor), defines strong foliation
GD30b	5078.5	bt	Pelite	300–2250	500–354	Reddish brown	None observed	Minor zrn	Internally unstrained, defines strong foliation
GD30m	5078.5	musc	Pelite	250–1250	500–354	Colourless	None observed	None observed	Thin interlayered biotite (minor), defines strong foliation

[a] ilm=ilmenite, gr=graphite, tur=tourmaline, zrn=zircon, hem=hematite.
[b] Bimodal grain size distribution.

5.3. Methodology

Muscovite and biotite separates were prepared from bulk samples using standard crushing, sieving, electromagnetic and heavy liquid mineral separation techniques. Separates were hand picked to greater than 99% purity. Sample weights were recorded and samples were packaged into aluminum foil containers along with four intercalated flux monitor standards of GA1550 biotite (age=98.8±0.5 Ma; Renne et al., 1998) and K_2SO_4 salts to determine correction factors for K-produced ^{40}Ar. Samples were sealed in a cadmium-lined canister to minimize $^{40}Ar_K$ production and irradiated in the McMaster Reactor, Canada (Berger and York, 1970). Correction factors for interfering reactions are: $(^{36}Ar/^{37}Ar)_{Ca}=2.70\ (\pm 0.05)\times 10^{-4}$; $(^{39}Ar/^{37}Ar)_{Ca}=.79\ (\pm 0.05)\times 10^{-4}$ and $(^{40}Ar/^{39}Ar)_K=.00\ (\pm 2.25)\times 10^{-4}$.

Irradiated samples, flux monitors, and atmospheric blanks were analyzed at the School of Earth Sciences, University of Melbourne. Samples were step-heated at 15–250 °C increments between 550 and 1350 °C and standards were fused at 1350 °C in a double vacuum tantalum furnace. Furnace temperatures are calibrated to ±2 °C. Liberated gas was purified by SAES Zr–Al getters. Argon isotopic analyses were conducted on a VG3600 mass spectrometer using a Daly detector. Mass

Table 3
^{40}Ar / ^{39}Ar age data from Kampa Dome

Sample: Gb 23b J=0.0035318±0.746%

Temp	^{40}Ar (mol)	^{40}Ar/^{39}Ar	±1σ	^{38}Ar/^{39}Ar	±1σ	^{37}Ar/^{39}Ar	±1σ	^{36}Ar/^{39}Ar	±1σ	^{39}Ar released (%)	K/Ca	±1σ	^{40}Ar* (%)	Age (Ma)	±1σ
550	1.50E−13	7.736345641	0.238	0.00000	9443.501	0.03316	0.769	0.014544498	1.143	0.0251	17.23	0.77	44.442	21.61	0.32
600	9.51E−14	3.901353847	0.256	0.00114	14.085	0.03235	0.569	0.004666137	1.068	0.0567	17.67	0.57	64.649	15.88	0.11
650	1.48E−13	2.848913627	0.222	0.00027	26.911	0.02959	0.733	0.001816927	2.753	0.1239	19.31	0.73	81.139	14.56	0.10
675	1.21E−13	2.546854734	0.167	0.00095	7.375	0.02434	0.545	0.000930569	3.503	0.1854	23.47	0.54	89.185	14.31	0.07
700	1.14E−13	2.457307425	0.185	0.00068	16.462	0.02156	1.174	0.000731718	3.837	0.2456	26.51	1.17	91.181	14.12	0.06
725	1.06E−13	2.478861465	0.165	0.00069	17.056	0.01870	1.128	0.000819251	3.511	0.3011	30.55	1.13	90.214	14.09	0.06
750	9.42E−14	2.427024513	0.170	0.00103	10.719	0.01594	1.026	0.000692639	6.663	0.3514	35.84	1.03	91.547	14.00	0.09
775	7.74E−14	2.438967753	0.182	0.00082	15.944	0.01396	3.125	0.000745541	6.238	0.3925	40.92	3.12	90.948	13.97	0.09
810	7.01E−14	2.505976514	0.148	0.00053	22.582	0.01443	1.624	0.001020224	3.843	0.4287	39.60	1.62	87.951	13.89	0.08
850	6.67E−14	2.599902491	0.223	0.00085	9.240	0.01518	1.469	0.001147399	4.944	0.4620	37.64	1.47	86.941	14.24	0.11
900	7.97E−14	2.618598973	0.174	0.00077	12.301	0.01499	0.909	0.001021742	7.668	0.5014	38.13	0.91	88.452	14.59	0.15
950	1.53E−13	2.603387962	0.191	0.00041	23.644	0.00939	1.566	0.001125768	3.006	0.5774	60.89	1.57	87.204	14.30	0.07
1000	2.78E−13	2.495318927	0.191	0.00038	19.255	0.00506	1.500	0.000852385	2.850	0.7215	112.83	1.50	89.887	14.13	0.05
1050	2.78E−13	2.481797308	0.178	0.00057	14.881	0.00613	0.978	0.000675205	1.935	0.8667	93.28	0.98	91.941	14.37	0.04
1100	2.18E−13	2.596705799	0.186	0.00100	10.713	0.01280	0.808	0.000660541	3.252	0.9752	44.65	0.81	92.464	15.12	0.05
1150	7.23E−14	4.244728465	0.233	0.00395	6.371	0.05136	1.293	0.000757484	11.767	0.9973	11.12	1.29	94.716	25.25	0.18
1250	6.70E−14	33.12332844	0.373	0.00002	4429.863	0.30243	1.497	0.023221041	2.399	0.9999	1.89	1.50	79.283	158.85	1.12
1350	4.52E−14	847.6764578	3.035	0.00075	1633.721	0.00240	32.759	0.000749719	5.477	1.0000	237.88	32.76	99.974	2487.55	40.97

Total fusion age=15.36±0.50 Ma   Preferred mean age=14.22±0.18 Ma (steps 650–1250, 81% of ^{39}Ar released)

Sample: GD 08b J=0.0035039±0.456%

Temp	^{40}Ar (mol)	^{40}Ar/^{39}Ar	±1σ	^{38}Ar/^{39}Ar	±1σ	^{37}Ar/^{39}Ar	±1σ	^{36}Ar/^{39}Ar	±1σ	^{39}Ar released (%)	K/Ca	±1σ	^{40}Ar* (%)	Age (Ma)	±1σ
550	4.32E−14	9.187427169	0.296	8.5085E−06	2989.945	0.024508724	6.010	0.024406538	1.340	0.0041	23.32	6.01	21.499	12.44	0.60
600	3.87E−14	4.053643386	0.225	4.1859E−06	4348.762	0.010547888	3.328	0.006679613	1.846	0.0126	54.17	3.33	51.301	13.10	0.23
650	1.04E−13	3.073613237	0.163	1.1806E−06	7329.471	0.003804937	2.663	0.00254911	2.034	0.0425	150.18	2.66	75.480	14.61	0.10
700	2.31E−13	2.736971921	0.154	0.00031552	50.019	0.002169666	3.791	0.000718985	90.802	0.1168	263.37	3.79	92.221	14.70	0.10
725	2.06E−13	2.493045966	0.160	0.00089076	7.943	0.00160979	3.818	0.000577254	5.183	0.1899	354.97	3.82	93.139	14.62	0.06
750	1.85E−13	2.437736245	0.172	0.00034894	19.748	0.002023522	3.558	0.000387455	6.770	0.2567	282.39	3.56	95.284	14.63	0.06
775	1.45E−13	2.447569612	0.157	0.00037445	24.862	0.002311175	4.623	0.000405708	2.989	0.3090	247.25	4.62	95.082	14.65	0.03
815	1.45E−13	2.475340261	0.141	0.00017044	42.031	0.003609411	3.596	0.000380477	6.574	0.3606	158.32	3.60	95.439	14.88	0.05
865	1.93E−13	2.451009117	0.156	0.00044703	15.500	0.003310602	1.208	0.000460356	4.395	0.4302	172.61	1.21	94.431	14.57	0.04
920	2.25E−13	2.450089289	0.164	5.0187E−05	192.638	0.002956048	3.259	0.000431011	4.189	0.5114	193.31	3.26	94.782	14.62	0.04
980	4.69E−13	2.387656441	0.154	4.1817E−06	2050.891	0.001491089	3.750	0.000209873	31.503	0.6847	383.23	3.75	97.382	14.64	0.12
1040	4.43E−13	2.387228323	0.176	0.00046742	12.129	0.002047438	3.184	0.000285921	6.563	0.8485	279.09	3.18	96.441	14.50	0.04
1100	2.94E−13	2.402509673	0.173	0.00109936	6.971	0.003167032	2.106	0.000230839	13.379	0.9563	180.43	2.11	97.141	14.70	0.06
1180	1.04E−13	2.541568944	0.162	0.00171286	5.578	0.006650699	5.267	0.000428538	10.425	0.9924	85.92	5.27	94.999	15.20	0.09
1260	2.26E−14	3.955088737	0.218	7.0007E−06	5033.228	0.034633564	1.762	6.99979E−06	67.414	0.9975	16.50	1.76	99.935	24.82	0.05
1350	2.47E−14	8.618623316	0.186	1.1348E−05	7925.503	0.077927184	3.616	0.00234939	10.556	1.0000	7.33	3.62	91.939	49.41	0.46

Total fusion age=14.77±0.81 Ma   Weighted mean age=14.64±0.15 Ma (steps 650–1100, Includes 94.4% of the ^{39}Ar)

Sample: GD 08m $J=0.0035060\pm0.492\%$

Temp	^{40}Ar (mol)	^{40}Ar/^{39}Ar	±1σ	^{38}Ar/^{39}Ar	±1σ	^{37}Ar/^{39}Ar	±1σ	^{36}Ar/^{39}Ar	±1σ	^{39}Ar released (%)	K/Ca	±1σ	^{40}Ar* (%)	Age (Ma)	±1σ
550	3.23E−14	14.77852843	0.277	1.8299E−05	1979.133	0.007894802	3.785	0.043154318	1.375	0.0020	72.38	3.79	13.712	12.77	1.10
650	5.07E−14	5.371362297	0.230	4.2402E−06	11830.052	0.01179138	6.508	0.010254665	1.461	0.0105	48.46	6.51	43.581	14.75	0.28
700	7.27E−14	5.11614702	0.165	2.8143E−06	7236.710	0.006044428	4.348	0.009535998	1.550	0.0233	94.54	4.35	44.917	14.48	0.28
750	2.05E−13	5.602140013	0.156	1.091E−06	9962.374	0.003908706	3.430	0.01089495	0.977	0.0563	146.19	3.43	42.528	15.01	0.20
800	7.89E−13	3.123507625	0.158	1.5837E−07	86252.070	0.000528775	24.267	0.002693285	1.317	0.2840	1080.66	24.27	74.508	14.66	0.07
825	5.96E−13	2.544475807	0.167	1.7064E−07	35665.600	0.000760173	5.203	0.000685795	3.267	0.4954	751.71	5.20	92.018	14.75	0.05
845	3.18E−13	2.456644609	0.139	0.00022921	31.921	0.000897202	4.911	0.000459548	3.844	0.6120	636.90	4.91	94.453	14.62	0.04
865	2.29E−13	2.462406251	0.159	4.2937E−07	18010.926	0.001200042	2.891	0.000475877	3.249	0.6960	476.17	2.89	94.270	14.63	0.04
885	1.67E−13	2.504301828	0.210	5.9815E−07	13588.652	2.84203E−06	3.500	0.000632894	3.606	0.7563	201063.79	3.50	92.514	14.60	0.05
920	1.43E−13	2.586028518	0.161	7.2225E−07	10714.760	0.004728187	2.099	5.7508E−05	67.097	0.8062	120.86	2.10	99.324	16.18	0.08
970	1.19E−13	2.748961855	0.170	9.2738E−07	8940.669	4.40632E−06	2.474	0.001127662	1.125	0.8451	129683.91	2.47	87.862	15.22	0.04
1040	2.01E−13	2.82328301	0.167	5.617E−07	10330.081	0.003856248	2.738	0.001668461	1.529	0.9093	148.18	2.74	82.522	14.68	0.06
1120	2.29E−13	2.527577098	0.167	4.4107E−07	15225.599	0.003898897	2.998	8.54515E−05	28.954	0.9910	146.56	3.00	98.981	15.76	0.05
1200	3.02E−14	3.042806424	0.261	4.0279E−06	1533.871	0.00247439	31.550	3.35925E−06	44.183	1.0000	230.94	31.55	99.951	19.14	0.05

Total fusion age = 14.90 ± 1.37 Ma Weighted mean plateau age = 14.65 ± 0.08 Ma (steps 550–885, includes 75.6% ^{39}Ar released)

Sample: GD 12 $J=0.0035194\pm0.628\%$

Temp	^{40}Ar (mol)	^{40}Ar/^{39}Ar	±1σ	^{38}Ar/^{39}Ar	±1σ	^{37}Ar/^{39}Ar	±1σ	^{36}Ar/^{39}Ar	±1σ	^{39}Ar released (%)	K/Ca	±1σ	^{40}Ar* (%)	Age (Ma)	±1σ
550	4.24E−14	4.831723569	0.246	4.5568E−06	9827.81	0.01575786	4.695	0.007931766	25.452	0.0069	36.26	4.69	51.485	15.73	3.76
650	6.42E−14	3.366796984	0.230	2.0973E−06	7465.87	0.008155447	5.314	0.002124363	7.655	0.0220	70.07	5.31	81.343	17.31	0.31
700	6.33E−14	3.079359272	0.178	1.9468E−06	16 871.99	0.010856921	2.912	0.001953807	2.185	0.0382	52.63	2.91	81.238	15.82	0.09
750	9.02E−14	3.230113275	0.149	1.4328E−06	91 45.79	0.006112971	2.654	0.001795394	2.512	0.0603	93.48	2.65	83.562	17.06	0.09
775	1.10E−13	3.739739682	0.188	1.3539E−06	70 63.10	6.56091E−06	3.509	0.002306053	2.390	0.0837	87095.93	3.65	81.768	19.31	0.11
800	2.91E−13	4.024030421	0.153	5.5224E−07	17 651.89	0.001545194	5.279	0.001670224	1.896	0.1409	369.81	5.28	87.724	22.28	0.07
825	5.81E−13	3.724052801	0.144	2.5619E−07	27 871.02	0.001161914	2.587	0.000923399	3.566	0.2643	491.80	2.59	92.660	21.78	0.07
845	5.46E−13	3.409678031	0.161	2.4965E−07	31 445.35	0.000927518	3.869	0.000515153	3.745	0.3909	616.08	3.87	95.521	20.56	0.05
856	4.41E−13	3.270322398	0.162	2.9633E−07	27 619.91	0.003948356	1.820	0.000125029	13.044	0.4976	144.73	1.82	98.855	20.41	0.04
885	3.13E−13	3.247616966	0.151	4.1457E−07	15 546.40	0.002534102	4.235	9.9729E−05	16.666	0.5739	225.50	4.23	99.077	20.32	0.04
910	2.47E−13	3.178379047	0.169	5.1567E−07	16 696.34	2.49899E−06	1.903	0.000260926	6.507	0.6352	228664.23	5.23	97.559	19.58	0.05
960	2.49E−13	3.108369754	0.201	5.0002E−07	20 282.94	2.42314E−06	6.725	0.000580544	8.924	0.6984	235821.70	6.23	94.466	18.55	0.10
1020	2.41E−13	3.125669288	0.149	5.1971E−07	16 832.85	2.51856E−06	10.162	0.000872491	1.732	0.7592	226887.19	7.23	91.737	18.12	0.04
1100	5.38E−13	3.132486114	0.142	2.3278E−07	25 770.85	0.001127299	3.468	0.000530826	4.413	0.8950	506.90	3.47	94.977	18.79	0.05
1180	2.09E−13	3.22090909	0.165	6.159E−07	13 578.39	0.000438932	47.253	1.86043E−05	92.828	0.9464	1301.86	47.25	99.814	20.30	0.05
1260	1.14E−13	3.607573729	0.172	1.2645E−06	61 13.39	6.12767E−06	3.478	0.000156231	24.221	0.9714	93253.75	3.48	98.707	22.47	0.08
1350	1.42E−13	3.919167081	0.145	1.1042E−06	11 723.01	5.3509E−06	49.205	1.10258E−06	6.866	1.0000	106791.08	49.20	99.979	24.71	0.04

Total fusion age = 20.09 ± 4.82 Ma Preferred mean age = 19.9 ± 1.0 Ma (steps 800–1100, includes 81.1% of the ^{39}Ar)

Sample: GD 23b $J=0.0035318\pm0.746\%$

Temp	^{40}Ar (mol)	^{40}Ar/^{39}Ar	±1σ	^{38}Ar/^{39}Ar	±1σ	^{37}Ar/^{39}Ar	±1σ	^{36}Ar/^{39}Ar	±1σ	^{39}Ar released (%)	K/Ca	±1σ	^{40}Ar* (%)	Age (Ma)	±1σ
550	2.10E−13	8.707071219	0.194	1.6579E−06	11 564.04	0.011203342	29.126	0.024016012	0.993	0.0155	51.01	29.13	18.494	10.23	0.45
650	2.03E−13	3.147716319	0.162	4.9825E−07	16 480.49	0.005733432	2.459	0.002821382	2.764	0.0569	99.67	2.46	73.502	14.68	0.15
675	2.01E−13	2.561746835	0.187	0.00058995	16.20	0.005236554	9.292	0.000238737	13.348	0.1074	109.12	9.29	97.227	15.80	0.07

(continued on next page)

Table 3 (*continued*)

Sample: Gb 23b

$J = 0.0035318 \pm 0.746\%$

Temp	^{40}Ar (mol)	^{40}Ar/^{39}Ar	±1σ	^{38}Ar/^{39}Ar	±1σ	^{37}Ar/^{39}Ar	±1σ	^{36}Ar/^{39}Ar	±1σ	^{39}Ar released (%)	K/Ca	±1σ	^{40}Ar* (%)	Age (Ma)	±1σ
695	2.05E−13	2.439014747	0.161	0.00079203	9.59	0.003878202	10.834	0.000129942	15.152	0.1614	147.34	10.83	98.406	15.23	0.04
710	2.59E−13	2.393094657	0.168	0.00052283	13.77	0.002210759	21.181	0.000230443	10.553	0.2311	258.48	21.18	97.134	14.75	0.05
730	2.11E−13	2.383478451	0.185	0.00075795	10.30	0.002794345	23.283	0.000131987	6.853	0.2880	204.49	23.28	98.343	14.88	0.03
760	1.79E−13	2.409123779	0.163	0.00066884	13.28	0.00207379	43.673	0.000401513	5.287	0.3358	275.55	43.67	95.055	14.54	0.05
800	1.52E−13	2.454678708	0.143	0.00070497	11.07	2.20497E−05	139.91	0.000547972	5.427	0.3758	25 915.54	139.91	93.384	14.55	0.06
840	1.43E−13	2.449406031	0.175	0.00068219	11.43	0.001633101	51.944	0.000568468	7.797	0.4132	349.90	51.94	93.123	14.48	0.09
880	1.56E−13	2.468544673	0.151	0.00040176	19.07	0.00501266	13.894	0.000315336	5.945	0.4539	114.00	13.89	96.206	15.07	0.04
910	2.12E−13	2.437905172	0.147	0.00039533	20.31	0.00563045	9.591	0.000218757	7.308	0.5100	101.49	9.59	97.328	15.06	0.04
930	2.65E−13	2.389934952	0.140	0.00051031	13.34	0.001942156	23.277	0.00025962	8.931	0.5813	294.22	23.28	96.770	14.68	0.05
945	2.80E−13	2.373173904	0.178	0.00058235	14.69	0.002620266	11.437	8.56257E−05	41.621	0.6571	218.08	11.44	98.913	14.90	0.07
960	2.65E−13	2.371282879	0.167	0.00059926	14.83	0.003849131	18.058	0.000191784	18.975	0.7290	148.46	18.06	97.589	14.69	0.07
975	2.32E−13	2.369730036	0.159	0.00077533	10.51	0.003355255	7.027	0.000191368	11.576	0.7919	170.31	7.03	97.593	14.68	0.05
995	1.95E−13	2.372485859	0.197	0.0008922	6.71	0.00302232	7.183	0.000101734	13.413	0.8447	189.07	7.18	98.712	14.86	0.04
1015	1.76E−13	2.388014104	0.177	0.00051891	75.84	0.004044448	19.938	4.86484E−07	647.98	0.8921	141.29	19.94	99.973	15.15	0.03
1040	1.86E−13	2.394626488	0.134	0.00014852	74.96	0.000585907	53.569	0.000307943	7.579	0.9420	975.29	53.57	96.180	14.62	0.05
1070	1.12E−13	2.420321434	0.169	0.00030962	26.33	0.006547032	32.061	0.000443396	13.215	0.9718	87.28	32.06	94.567	14.53	0.11
1100	7.14E−14	2.472009836	0.137	0.00104619	5.86	0.012020977	19.758	1.18875E−06	67.770	0.9904	47.54	19.76	99.966	15.68	0.02
1180	2.50E−14	3.03407211	0.225	0.00189044	18.72	0.031816859	15.911	0.000652733	28.490	0.9957	17.96	15.91	93.627	18.01	0.35
1350	5.14E−14	7.721487894	0.204	0.00336204	6.16	0.052161286	10.659	0.014361889	7.065	1.0000	10.96	10.66	45.034	22.02	1.89

Total fusion age = 14.84 ± 1.49 Ma

Preferred mean age = 14.91 ± 0.26 Ma (steps 650 to 1070, 95.6% ^{39}Ar released)

Sample: GD 23m

$J = 0.0035443 \pm 0.864\%$

Temp	^{40}Ar (mol)	^{40}Ar/^{39}Ar	±1σ	^{38}Ar/^{39}Ar	±1σ	^{37}Ar/^{39}Ar	±1σ	^{36}Ar/^{39}Ar	±1σ	^{39}Ar released (%)	K/Ca	±1σ	^{40}Ar* (%)	Age (Ma)	±1σ
550	5.10E−14	14.79069763	0.185	1.1608E−05	2360.7046	0.025831542	27.827239	4.067E−02	1.0561932	0.0022	22.12	27.83	18.74	17.63	0.81
675	6.90E−14	5.075757667	0.228	0.00047395	48.979861	0.019813522	22.488825	8.886E−03	2.1417955	0.0107	28.84	22.49	48.26	15.60	0.36
750	2.10E−13	6.961629958	0.178	0.00035521	33.818194	0.023949592	8.2197796	1.562E−02	0.7525694	0.0298	23.86	8.22	33.69	14.93	0.23
775	3.72E−13	5.41182922	0.156	0.00033506	28.087129	0.010340844	10.314487	1.035E−02	0.4583536	0.0730	55.26	10.31	43.50	14.99	0.10
795	5.40E−13	3.218445387	0.159	0.00022164	25.288226	0.010393234	6.9069936	2.990E−03	0.9284817	0.1788	54.98	6.91	72.53	14.87	0.06
815	5.88E−13	2.638772232	0.173	0.00043878	14.98626	0.008522794	6.6800788	2.504E−04	5.9166028	0.3193	67.05	6.68	97.18	16.33	0.04
840	6.57E−13	2.478510194	0.161	0.00055273	11.68716	0.007125625	8.0891567	6.392E−04	2.3097244	0.4863	80.19	8.09	92.36	14.58	0.04
865	5.09E−13	2.416314488	0.170	0.00049393	16.416814	0.008302309	5.3274652	4.762E−04	2.6485962	0.6191	68.83	5.33	94.16	14.49	0.03
890	3.26E−13	2.450936421	0.197	0.0007041	8.0076285	0.008393316	4.6465605	5.776E−04	4.0268255	0.7029	68.08	4.65	93.02	14.52	0.05
920	2.85E−13	2.525844874	0.160	0.00043469	17.412603	0.004353128	18.485637	2.176E−04	14.420031	0.7739	131.27	18.49	97.44	15.67	0.06
950	1.75E−13	2.656632514	0.242	0.00064906	17.090744	0.004398124	30.310165	1.194E−03	4.6138682	0.8155	129.93	30.31	86.70	14.67	0.11
1000	1.70E−13	2.82223079	0.179	0.0002526	73.431199	0.005685569	21.191048	1.838E−03	3.3475379	0.8536	100.51	21.19	80.74	14.51	0.12
1060	2.73E−13	2.809086076	0.225	0.00012553	48.893064	0.004283809	13.73823	1.747E−03	2.4418382	0.9149	133.39	13.74	81.61	14.60	0.09
1130	3.10E−13	2.481611427	0.275	0.00021652	29.225681	0.004906452	31.296446	6.500E−04	3.5974951	0.9937	116.46	31.30	92.24	14.58	0.06
1350	4.90E−14	4.880841465	0.284	0.00262171	7.1808376	0.022025862	25.696603	8.820E−03	4.2471467	1.0000	25.94	25.70	46.60	14.49	0.70

Total fusion age = 14.96 ± 1.11 Ma

Weighted mean age = 14.65 ± 0.39 Ma (steps 840–1130, includes 67.4% ^{39}Ar released)

Sample: GD 25 $J=0.0035568\pm0.982\%$

Temp	^{40}Ar (mol)	^{40}Ar/^{39}Ar	±1σ	^{38}Ar/^{39}Ar	±1σ	^{37}Ar/^{39}Ar	±1σ	^{36}Ar/^{39}Ar	±1σ	^{39}Ar released (%)	K/Ca	±1σ	^{40}Ar* (%)	Age (Ma)	±1σ
550	4.20E−13	11.96564832	0.1778145	1.139E−06	15256.193	0.020746688	1.5626701	0.035799135	0.9816325	0.0318	27.54	1.56	11.59	8.88	0.67
600	2.39E−13	4.550999363	0.1904053	0.00111869	7.1876989	0.009730013	1.5455689	0.008658469	0.7983745	0.0792	58.73	1.55	43.78	12.74	0.14
650	2.51E−13	2.954985603	0.1688403	0.00067852	12.896995	0.005357861	1.3393536	0.002760876	1.2808837	0.1560	106.65	1.34	72.38	13.67	0.07
675	2.74E−13	2.535054791	0.1687958	0.00074908	9.4349789	0.003647922	1.8675113	9.24828E−05	62.37351	0.2538	156.64	1.87	98.90	16.02	0.11
700	2.75E−13	2.371754365	0.1480054	0.00103741	8.141688	0.002790444	1.575336	0.000711846	3.387397	0.3587	204.78	1.58	91.11	13.82	0.05
725	2.38E−13	2.326586335	0.1809365	0.00088213	13.249399	0.002382099	3.2961127	0.000608275	3.0190084	0.4513	239.88	3.30	92.25	13.72	0.04
750	1.85E−13	2.337381533	0.1636071	0.00113727	6.6192073	0.003090661	2.8204783	0.000615268	3.6124932	0.5228	184.89	2.82	92.20	13.78	0.05
775	1.27E−13	2.420364188	0.1574341	0.00147741	4.8641591	0.003758083	2.8458358	0.000977231	4.7613797	0.5701	152.05	2.85	88.05	13.63	0.09
800	9.15E−14	2.612759983	0.1778806	0.00131632	6.211624	0.005268182	2.0770332	0.00114154	7.0209415	0.6018	108.47	2.08	87.07	14.54	0.15
830	9.74E−14	2.771407036	0.1409806	0.00081897	18.623877	0.006515242	4.7705706	0.002038539	3.6593127	0.6336	87.71	4.77	78.25	13.87	0.14
860	1.18E−13	2.609036233	0.204265	0.00087702	11.279252	0.004606959	4.076616	0.001639031	2.8232675	0.6746	124.04	4.08	81.42	13.58	0.09
900	2.14E−13	2.396207137	0.1583938	0.00051554	13.538399	0.002979976	1.2116519	0.000881189	2.547879	0.7553	191.76	1.21	89.11	13.65	0.05
940	2.64E−13	2.351290627	0.1567538	0.0007222	10.355071	0.001798541	3.4706602	0.000718572	3.865291	0.8569	317.72	3.47	90.95	13.67	0.06
980	1.63E−13	2.433025196	0.1399778	0.00129675	6.0710543	0.001918492	4.5546903	0.000902468	3.7149922	0.9175	297.85	4.55	89.02	13.85	0.07
1020	1.05E−13	2.508072629	0.1633059	0.00155439	4.6926081	0.002382692	2.4480288	0.001318436	2.5781371	0.9554	239.82	2.45	84.45	13.54	0.07
1070	8.29E−14	2.529562418	0.1835883	0.00058767	16.738768	0.002431943	4.066224	0.001209339	3.7295442	0.9851	234.97	4.07	85.86	13.89	0.09
1140	3.01E−14	2.934671922	0.4666553	0.00090871	37.405408	0.021779419	5.4560255	3.90214E−06	31.14452	0.9943	26.24	5.46	99.94	18.73	0.09
1250	1.96E−14	4.571459295	0.3419778	7.5896E−06	4920.3755	0.014449129	6.0329044	0.002122107	7.9961245	0.9982	39.55	6.03	86.27	25.13	0.33
1350	2.19E−14	11.11506434	1.5060431	2.0331E−05	3360.1638	0.078636098	3.8003914	0.000336725	168.98266	1.0000	7.27	3.80	99.10	69.34	1.46

Total fusion age = 13.96 ± 1.16 Ma   Weighted mean age = 13.74 ± 0.28 Ma (steps 725–1070, includes 73.1% of the ^{39}Ar released)

Sample: GD 26 $J=0.0035601\pm0.484\%$

Temp	^{40}Ar (mol)	^{40}Ar/^{39}Ar	±1σ	^{38}Ar/^{39}Ar	±1σ	^{37}Ar/^{39}Ar	±1σ	^{36}Ar/^{39}Ar	±1σ	^{39}Ar released (%)	K/Ca	±1σ	^{40}Ar* (%)	Age (Ma)	±1σ
550	2.05E−13	15.23358238	0.1649992	2.9677E−06	6285.357	0.018531239	29.35592	0.046072056	0.7837333	0.0137	30.84	29.36	10.63	10.37	0.69
600	1.61E−13	7.133647396	0.198749	0.00101179	16.891718	0.002495889	105.34359	0.017260201	0.6622544	0.0366	228.95	105.34	28.50	13.01	0.22
650	2.03E−13	3.903254655	0.1867425	0.00024831	33.120555	0.004912841	20.624946	0.005955804	0.570581	0.0897	116.31	20.62	54.90	13.71	0.08
675	1.69E−13	2.783490284	0.1774021	0.00059752	10.746801	0.00531188	14.702132	0.002130253	2.0510907	0.1515	107.58	14.70	77.37	13.78	0.09
700	1.78E−13	2.49708357	0.1589582	0.00058404	14.847132	0.003786771	13.50303	0.001144523	2.3314653	0.2240	150.90	13.50	86.44	13.81	0.06
725	2.06E−13	2.37540963	0.2071711	0.00061645	11.823827	0.004541448	10.868855	0.000748794	4.4249587	0.3122	125.83	10.87	90.67	13.78	0.07
750	2.20E−13	2.327493897	0.1998752	0.00071337	9.9801762	0.002595256	14.737344	0.00055131	4.3096765	0.4082	220.18	14.74	92.98	13.85	0.05
775	1.77E−13	2.35001164	0.190039	0.00090236	6.9764263	0.001643378	12.016379	0.000624967	3.6862385	0.4848	347.72	12.02	92.12	13.85	0.05
800	1.27E−13	2.459091347	0.1559722	0.00085322	12.090207	0.005816112	21.57294	0.001024122	2.4018026	0.5372	98.25	21.57	87.68	13.80	0.05
850	1.26E−13	2.694640505	0.2476715	0.00088194	6.7671917	0.004917652	13.662778	0.001815745	1.4818402	0.5848	116.20	13.66	80.07	13.81	0.07
900	1.91E−13	2.462000457	0.1657922	0.00036191	19.031576	0.00485468	9.5776044	0.001065742	2.3801552	0.6639	117.71	9.58	87.19	13.74	0.05
940	3.29E−13	2.309013286	0.1593778	0.00037205	27.59815	0.004545577	9.388659	0.000240389	6.5968955	0.8091	125.71	9.39	96.90	14.32	0.04
980	2.56E−13	2.321059733	0.1397598	0.00063319	11.150697	0.002983066	11.649829	0.000573909	1.2315795	0.9212	191.56	11.65	92.67	13.77	0.02
1020	1.16E−13	2.482204896	0.1938076	0.00162966	6.598401	0.003131383	50.327115	0.000965511	4.9459625	0.9687	182.48	50.33	88.49	14.06	0.09
1080	5.96E−14	2.568266915	0.1891631	0.00172355	9.1453059	0.007530421	7.2497737	0.00157721	3.9156507	0.9923	75.88	7.25	81.84	13.45	0.12
1140	1.77E−14	3.872167978	0.2660785	0.00412812	9.0377036	0.033562425	33.962103	0.00573261	7.6059844	0.9970	17.03	33.96	56.24	13.94	0.82
1240	1.80E−14	9.2016912	0.3420083	0.00087374	129.75822	0.000647546	20.909003	0.021999694	6.4889795	0.9989	882.45	20.91	29.35	17.26	2.68
1350	2.72E−14	26.34003228	0.4740213	3.8772E−05	3839.767	0.001226517	168.45374	0.081856431	1.2463938	1.0000	465.90	168.45	8.17	13.77	1.81

Total fusion age = 13.82 ± 3.09   Weighted mean plateau age = 13.80 ± 0.07 Ma (steps 650–900, includes 62.7% of the ^{39}Ar released)

(continued on next page)

Table 3 (*continued*)

Sample: Gb 23b $J = 0.0035318 \pm 0.746\%$

Temp	^{40}Ar (mol)	^{40}Ar/^{39}Ar	±1σ	^{38}Ar/^{39}Ar	±1σ	^{37}Ar/^{39}Ar	±1σ	^{36}Ar/^{39}Ar	±1σ	^{39}Ar released (%)	K/Ca	±1σ	^{40}Ar* (%)	Age (Ma)	±1σ
550	1.28E−13	14.27076229	0.222992	4.472E−06	5071.095	0.040524551	7.3498789	0.042305362	0.7652182	0.0063	14.10	7.35	12.40	11.34	0.62
600	1.11E−13	5.750915375	0.3022974	0.00075757	12.245786	0.094116082	4.1581786	0.012138606	0.7466289	0.0199	6.07	4.16	37.62	13.86	0.18
650	2.71E−13	3.668494198	0.1578493	0.00033163	17.291595	0.079253109	1.6459295	0.004611759	1.0171551	0.0720	7.21	1.65	62.84	14.77	0.09
675	3.00E−13	2.922834845	0.1636415	0.00076687	10.861098	0.069043784	1.0960554	0.00196178	1.2559197	0.1443	8.28	1.10	80.15	15.01	0.05
700	3.05E−13	2.667857454	0.1465266	0.00106223	5.4431747	0.025419572	2.212427	0.00103324	2.6618665	0.2250	22.48	2.21	88.54	15.13	0.06
725	2.94E−13	2.585132135	0.1552579	0.00108839	8.3185426	0.005247847	4.7572051	0.000656107	3.5362025	0.3051	108.89	4.76	92.48	15.31	0.05
750	2.44E−13	2.557825455	0.1478602	0.00127754	5.3525932	0.003316232	17.194084	0.000435864	2.4591796	0.3722	172.31	17.19	94.95	15.55	0.03
775	1.58E−13	2.552327816	0.190548	0.00166059	5.453195	0.0042731	26.299197	4.40074E−05	64.165072	0.4159	133.73	26.30	99.47	16.26	0.06
800	1.04E−13	2.584964997	0.2286339	0.00160142	6.0505192	0.005937091	23.878399	0.000347702	21.277866	0.4443	96.25	23.88	96.01	15.89	0.14
850	1.68E−13	2.571705315	0.1778215	0.00072068	11.914097	0.004402999	7.4777049	0.000396027	6.9297476	0.4903	129.78	7.48	95.43	15.72	0.06
900	2.01E−13	2.55240793	0.1670027	0.000858	8.6777177	0.005737423	2.4518697	0.000402409	4.5621393	0.5457	99.60	2.45	95.32	15.58	0.04
925	2.11E−13	2.524878605	0.136656	0.00100093	6.9527775	0.005501675	8.6442561	0.00011496	12.423261	0.6046	103.86	8.64	98.64	15.95	0.03
950	2.73E−13	2.485859388	0.1559804	0.00082392	10.366925	0.003783449	16.685146	0.000357005	4.5372353	0.6821	151.03	16.69	95.74	15.24	0.04
980	3.07E−13	2.476855315	0.1561776	0.0008788	9.5369544	0.004302609	4.8386639	0.000245609	3.49502	0.7693	132.81	4.84	97.05	15.40	0.03
1010	2.45E−13	2.485891823	0.1468193	0.00124484	4.7735614	0.005503353	4.8001116	0.00029017	5.1605092	0.8387	103.83	4.80	96.53	15.37	0.04
1040	2.32E−13	2.48719385	0.1692942	0.00118582	8.2416946	0.005139271	7.7988605	0.000438461	3.3306729	0.9045	111.19	7.80	94.77	15.10	0.04
1070	1.87E−13	2.513244328	0.1448354	0.00139407	5.5531784	0.008440442	7.3627557	0.000482165	4.6441374	0.9569	67.70	7.36	94.31	15.18	0.05
1110	1.21E−13	2.551753521	0.1739335	0.00176971	4.2266718	0.030705353	3.1439263	0.00062802	3.4023211	0.9904	18.61	3.14	92.71	15.15	0.05
1170	3.10E−14	3.142174665	0.3104087	0.00531188	6.0836628	0.000133281	60.06859	0.001250754	4.7455599	0.9974	4287.39	60.07	88.22	17.74	0.13
1350	3.21E−14	8.678184931	0.2039809	0.0015634	43.677522	0.028788623	36.769146	0.01979131	2.1021986	1.0000	19.85	36.77	32.61	18.11	0.79

Total fusion age = 15.35 ± 1.12 Ma

Preferred mean age = 15.42 ± 0.30 Ma (steps 650–1110, includes 97.1% of the ^{39}Ar)

Sample: GD 28m $J = 0.0035028 \pm 0.438\%$

Temp	^{40}Ar (mol)	^{40}Ar/^{39}Ar	±1σ	^{38}Ar/^{39}Ar	±1σ	^{37}Ar/^{39}Ar	±1σ	^{36}Ar/^{39}Ar	±1σ	^{39}Ar released (%)	K/Ca	±1σ	^{40}Ar* (%)	Age (Ma)	±1σ
550	2.91566E−14	18.3211181	0.3415761	2.5135E−05	3645.1043	0.001252243	34.761628	0.046705625	1.896665	0.0017	456.32	34.76	24.67	28.34	1.62
675	3.51039E−14	5.266586436	0.2139319	6.0011E−06	4524.216	0.022721794	22.108765	0.009185344	2.3804839	0.0090	25.15	22.11	48.46	16.06	0.41
750	1.23474E−13	7.466292626	0.1673184	0.00031011	22.770244	0.022240811	6.7235289	0.017549638	0.7051336	0.0269	25.69	6.72	30.54	14.35	0.24
775	2.94177E−13	4.988351102	0.2079634	0.00023633	47.453849	0.006503706	12.830208	0.008752893	0.7785241	0.0909	87.86	12.83	48.14	15.12	0.14
795	4.32241E−13	2.747366992	0.2163544	0.00017911	58.401949	0.005558788	23.509407	0.001099315	3.1454228	0.2617	102.80	23.51	88.16	15.24	0.07
815	3.3896E−13	2.470266492	0.2089336	0.00041623	16.713463	0.004773282	10.33348	0.000402455	3.5508564	0.4107	119.71	10.33	95.17	14.80	0.04
840	2.90001E−13	2.426848279	0.1621445	0.00047102	13.617656	0.002798147	21.276297	0.000309939	6.0928845	0.5404	204.22	21.28	96.21	14.70	0.04
865	2.30984E−13	2.441250157	0.1606028	0.00046365	13.170378	0.004323862	16.416282	0.000350652	7.2805429	0.6432	132.16	16.42	95.74	14.71	0.05
890	1.87902E−13	2.466980501	0.1590036	0.00041099	17.133198	0.008551464	4.8008735	0.000498038	6.6899019	0.7258	66.82	4.80	94.02	14.60	0.07
920	1.33827E−13	2.518938262	0.1599877	0.00071019	14.920041	0.014903943	25.560579	0.00070744	4.924588	0.7835	38.34	25.56	91.68	14.54	0.07
950	8.78229E−14	2.634406684	0.1623306	0.00092	12.277912	0.007661962	17.224402	0.000977804	4.5023566	0.8197	74.58	17.22	89.02	14.76	0.09
1000	8.17668E−14	2.748875146	0.1985132	0.00059096	24.260134	0.003291694	46.43778	0.001340013	2.2270011	0.8520	173.60	46.44	85.58	14.81	0.06
1060	1.25456E−13	2.75697208	0.2152674	0.00023269	41.162345	0.003695332	24.26019	0.001446046	1.7350088	0.9014	154.64	24.26	84.49	14.66	0.06
1130	1.81908E−13	2.570795924	0.1658321	0.00029703	26.808384	0.006948829	13.145444	0.000841076	3.3339355	0.9782	82.23	13.15	90.31	14.62	0.06
1350	8.16526E−14	4.071240767	0.1910893	0.00146401	5.6105232	0.011674363	22.891181	0.004402933	0.9823854	1.0000	48.95	22.89	68.03	17.42	0.09

Total fusion age = 14.90 ± 1.00

Weighted mean plateau age = 14.68 ± 0.07 Ma (steps 815–1130, includes 56.8% of ^{39}Ar released)

Sample: GD 30b   *J*=0.0035625±0.638%

Temp	^{40}Ar (mol)	^{40}Ar/^{39}Ar	±1σ	^{38}Ar/^{39}Ar	±1σ	^{37}Ar/^{39}Ar	±1σ	^{36}Ar/^{39}Ar	±1σ	^{39}Ar released (%)	K/Ca	±1σ	^{40}Ar* (%)	Age (Ma)	±1σ
550	5.92E−14	10.86778967	0.294	0.00001	5108.081	0.00024	192.879	3.024E−02	1.2930992	0.0041	2410.62	192.88	17.79	12.38	0.75
600	4.70E−14	4.612672687	0.242	0.00026	41.928	0.00774	13.269	8.206E−03	1.0210573	0.0118	73.79	13.27	47.43	14.01	0.17
650	1.44E−13	3.624159238	0.203	0.00015	50.126	0.00459	14.562	4.362E−03	1.5071374	0.0416	124.46	14.56	64.42	14.95	0.13
675	1.89E−13	2.944074402	0.168	0.00044	14.552	0.00459	9.910	2.015E−03	1.446156	0.0900	124.60	9.91	79.76	15.03	0.06
700	2.17E−13	2.654499209	0.138	0.00060	11.319	0.00240	42.595	8.542E−04	2.9116014	0.1516	238.51	42.59	90.47	15.37	0.05
725	2.44E−13	2.560644173	0.180	0.00058	13.319	0.00343	12.288	5.518E−04	2.1690228	0.2234	166.53	12.29	93.61	15.34	0.04
750	2.18E−13	2.528657615	0.158	0.00080	8.213	0.00417	9.272	4.535E−04	3.687591	0.2885	136.96	9.27	94.68	15.33	0.04
775	1.66E−13	2.54765682	0.156	0.00112	8.539	0.00583	16.837	4.917E−04	9.2661287	0.3377	98.01	16.84	94.28	15.37	0.09
800	1.11E−13	2.539928059	0.216	0.00108	14.119	0.00299	30.966	4.296E−04	14.869619	0.3707	190.81	30.97	94.98	15.44	0.13
850	1.51E−13	2.498077455	0.173	0.00043	17.386	0.00461	9.996	3.985E−04	3.3569142	0.4162	123.95	10.00	95.27	15.23	0.04
900	1.53E−13	2.480315046	0.172	0.00059	12.036	0.00291	22.514	3.536E−04	4.340347	0.4627	196.43	22.51	95.77	15.21	0.04
940	2.59E−13	2.479825075	0.143	0.00023	28.870	0.00612	8.032	4.189E−04	2.8053633	0.5414	93.38	8.03	94.99	15.08	0.03
980	4.28E−13	2.468288937	0.151	0.00044	17.184	0.00421	5.118	7.712E−05	7.0568822	0.6719	135.78	5.12	99.06	15.65	0.03
1020	3.88E−13	2.489189255	0.143	0.00000	27825.467	0.00357	7.004	1.358E−04	5.0963683	0.7893	160.02	7.00	98.37	15.67	0.03
1070	4.06E−13	2.503749985	0.145	0.00027	24.390	0.00301	7.488	3.692E−04	2.1501942	0.9115	189.63	7.49	95.62	15.33	0.03
1105	2.12E−13	2.544128489	0.152	0.00104	7.409	0.00445	7.525	4.071E−04	5.0643788	0.9742	128.34	7.52	95.25	15.51	0.05
1140	6.55E−14	2.716537816	0.199	0.00216	4.407	0.00729	40.128	9.727E−04	6.7727018	0.9924	78.33	40.13	89.40	15.54	0.13
1350	4.89E−14	4.811409153	0.219	0.00208	9.384	0.00639	44.182	7.480E−03	1.7029395	1.0000	89.37	44.18	54.06	16.64	0.25

Total fusion age=15.36±1.02 Ma   Weighted mean age=15.39±0.23 Ma (steps 650–1140, includes 98% of ^{39}Ar released)

Sample: GD 30m   *J*=0.0035672±0.946%

Temp	^{40}Ar (mol)	^{40}Ar/^{39}Ar	±1σ	^{38}Ar/^{39}Ar	±1σ	^{37}Ar/^{39}Ar	±1σ	^{36}Ar/^{39}Ar	±1σ	^{39}Ar released (%)	K/Ca	±1σ	^{40}Ar* (%)	Age (Ma)	±1ó
550	4.20E−14	14.00003951	0.304	0.00001	4630.700	0.01677	32.747	2.378E−02	11.469031	0.0029	34.07	32.75	49.80	44.32	5.06
650	4.37E−14	5.311304335	0.219	0.00144	10.944	0.00676	89.212	5.559E−03	5.8607188	0.0109	84.51	89.21	69.06	23.46	0.62
700	5.60E−14	4.650667367	0.196	0.00061	29.371	0.00836	59.667	1.013E−03	5.4530307	0.0226	68.32	59.67	93.55	27.79	0.12
750	1.61E−13	7.400811511	0.177	0.00084	18.629	0.00640	23.715	1.507E−02	2.1492915	0.0438	89.24	23.72	39.84	18.88	0.61
775	3.10E−13	4.828166362	0.149	0.00032	21.308	0.00396	16.915	7.777E−04	7.5472801	0.1062	144.24	16.92	95.23	29.35	0.12
800	2.99E−13	2.938001004	0.166	0.00106	6.753	0.00171	32.393	1.977E−03	1.3290009	0.2052	334.75	32.39	80.10	15.08	0.06
820	2.78E−13	2.560577149	0.249	0.00037	28.116	0.00291	11.824	4.076E−04	8.5784124	0.3109	196.20	11.82	95.28	15.64	0.08
845	2.46E−13	2.443990534	0.162	0.00000	23065.820	0.00465	3.614	1.190E−04	4.6712157	0.4089	123.01	3.61	98.54	15.44	0.03
870	3.22E−13	2.432992428	0.183	0.00033	24.748	0.00275	16.863	2.885E−04	5.2809293	0.5374	208.01	16.86	96.48	15.05	0.04
900	2.99E−13	2.456350681	0.181	0.00041	16.313	0.00274	13.699	9.379E−05	13.992173	0.6559	208.47	13.70	98.85	15.56	0.04
930	2.12E−13	2.49736994	0.159	0.00052	12.744	0.00375	16.384	1.873E−04	8.5642894	0.7383	152.18	16.38	97.76	15.65	0.04
970	1.55E−13	2.587539355	0.158	0.00067	14.993	0.00235	20.739	3.387E−04	15.78057	0.7965	243.50	20.74	96.11	15.94	0.10
1020	1.20E−13	2.745057666	0.169	0.00048	19.134	0.00197	45.724	1.304E−03	2.2783522	0.8390	289.56	45.72	85.94	15.12	0.06
1060	1.43E−13	2.739645223	0.193	0.00027	30.057	0.00412	5.639	7.947E−04	1.6527432	0.8897	138.64	5.64	91.41	16.05	0.04
1130	2.24E−13	2.571744494	0.143	0.00032	21.570	0.00441	19.225	1.678E−04	12.067718	0.9742	129.69	19.23	98.05	16.16	0.04
1250	6.16E−14	2.852618123	0.211	0.00221	4.603	0.02663	7.729	1.740E−03	3.5390107	0.9952	21.46	7.73	81.97	14.99	0.12
1350	3.18E−14	6.463600395	0.196	0.00263	13.298	0.00027	202.219	9.575E−03	6.2592695	1.0000	2092.21	202.22	56.22	23.24	1.13

Total fusion age=16.78±2.21 Ma   Preferred mean age=15.54±0.39 Ma (Steps 800–1250, includes 89% of ^{39}Ar released) discrimination was monitored using analyses of purified air aliquots from a Dorflinger pipette. Individual grains of GA1550 biotite were also analyzed by laser fusion on a VG5400 mass spectrometer using a Daly detector.

Isotopic data was corrected for mass spectrometer backgrounds, mass discrimination and fluence gradients. Errors in the age calculations are presented as 1σ uncertainties unless otherwise identified and exclude errors associated with *J*-values and decay constants (Steiger and Jäger, 1977).

Complete step-heating data and derived age spectra are presented in Table 3 and Fig. 5, respectively. A weighted mean plateau age is defined for samples where three or more successive steps comprising >50% of the total ^{39}Ar released have an age within 1σ error of the mean (McDougall and Harrison, 1999). Only three samples (GD 08m, 26, 28m) yielded spectra that fit this strict criterion. A weighted mean "pseudo-plateau" age is calculated where a series of concordant steps comprising >50% of the total ^{39}Ar released contain only one or two discordant steps. Weighted mean "pseudo-plateau" ages are reported for samples GD 08b, 23m, 25 and 30b. Preferred mean ages are reported for relatively discordant spectra where the criteria for calculating a mean plateau or weighted mean age was not met, but where successive steps comprising >50% of the total ^{39}Ar released yield individual ^{40}Ar/^{39}Ar ages within ~1 Ma of adjacent steps. Preferred ages are reported for samples GD 05, 12, 23b, 28b and 30m. Inverse isochron ages were determined from ^{36}Ar/^{40}Ar vs. ^{39}Ar/^{40}Ar inverse isochron plots of corrected isotopic data to evaluate whether the assumption that initial ^{40}Ar/^{36}Ar ratios were atmospheric (~295) was valid. Inverse isochron plots produced clusters of points proximal to the abscissa, poorly defined regression lines trending towards atmospheric values, and commonly large mean standard weighted deviations. These phenomena are as a result of low levels of atmospheric argon within the samples and low levels of background ^{36}Ar, as indicated by our blank measurements between sample runs. We do not consider the data to provide any additional information to the step heating spectra, and do not discuss them further.

5.4. ^{40}Ar/^{39}Ar results

Individual sample results are described in stratigraphic order, from the top of the metasedimentary sequence to the Kampa Granite.

5.4.1. GD 05

Biotite sample GD 05 (Fig. 5 a,b) yielded a saddle-shaped apparent age spectrum defined by anomalously old initial and final steps flanking a set of more concordant intermediate temperature steps (650 to 1050 °C). The discordancy between steps prohibited determination of a plateau age and the weighted mean age for the intermediate temperature steps (81% of the total ^{39}Ar) is calculated at 14.22±0.18 Ma. The total fusion age for the sample is 15.36±0.50 Ma. The K/Ca plot shows a weak inverse correlation with age, although all K/Ca ratios except for the last step are >15, as would be expected for clean biotite separates with minimal Ca contamination.

This spectrum exhibits two characteristics common to many biotite ^{40}Ar/^{39}Ar step-heating spectra worldwide (including the Himalaya; e.g., Maluski et al., 1988); a saddle shape and a series of discordant intermediate temperature steps. A variety of explanations for this non-systematic behavior exist, (1) incorporation of excess argon through intragrain diffusion (Harrison and McDougall, 1981; Pickles et al., 1997) or trapped within fluid inclusions and/or mineral phases (Kelley, 2002), (2) coexisting distinct biotite populations (York and Lopez Martinez, 1986), (3) recoil-induced ^{39}Ar$_K$ redistribution and differential release from interlayered chlorite (Lo and Onstott, 1989; Di Vincenzo et al., 2003) and / or other fine-grained minerals (Dong et al., 1997) during step-heating, and (4) deformation-induced dislocations or subgrain networks that alter argon diffusivity, retentivity and/or susceptibility to dehydroxylation reactions (Kramar et al., 2001; Mulch et al., 2002; Forster and Lister, 2004).

In support of the excess argon model, GD 05 biotites contain both fine-grained serrated grain boundaries (which may have rendered grain boundaries susceptible to incorporation of excess argon) and contain small mineral inclusions visible under 40× power (which may have hosted fluid inclusions). It is therefore possible that the anomalous low and high temperature step ^{40}Ar/^{39}Ar ages may have resulted from release of excess argon at low temperatures from the least retentive grain boundary sites (Harrison and McDougall, 1981) and at high temperatures from the more retentive mineral and fluid inclusion sites during step heating (Esser et al., 1997; Kelley, 2002). It is unlikely that the coexisting matrix and porphyroblastic biotite populations observed in GD 05 are to blame for the spectral discordancy, as careful sieving and handpicking included only clean biotite porphyroblasts of similar appearance in the analyzed fraction (Table 2). It is possible that irradiation-induced recoil of ^{39}Ar$_K$ nuclei into adjacent chlorite interlayers or quartz inclusions promoted argon release at different temperatures, resulting in the discordant intermediate temperature steps (Lo and Onstott, 1989; Di Vincenzo et al., 2003). We did not observe any chlorite alteration in this sample, although submicroscopic chlorite interlayers as small as 10 Å have been noted to influence biotite release spectra (Di Vincenzo et al., 2003). However, both the absence of any visible retrogression and the saddle shape of the spectrum, which differs

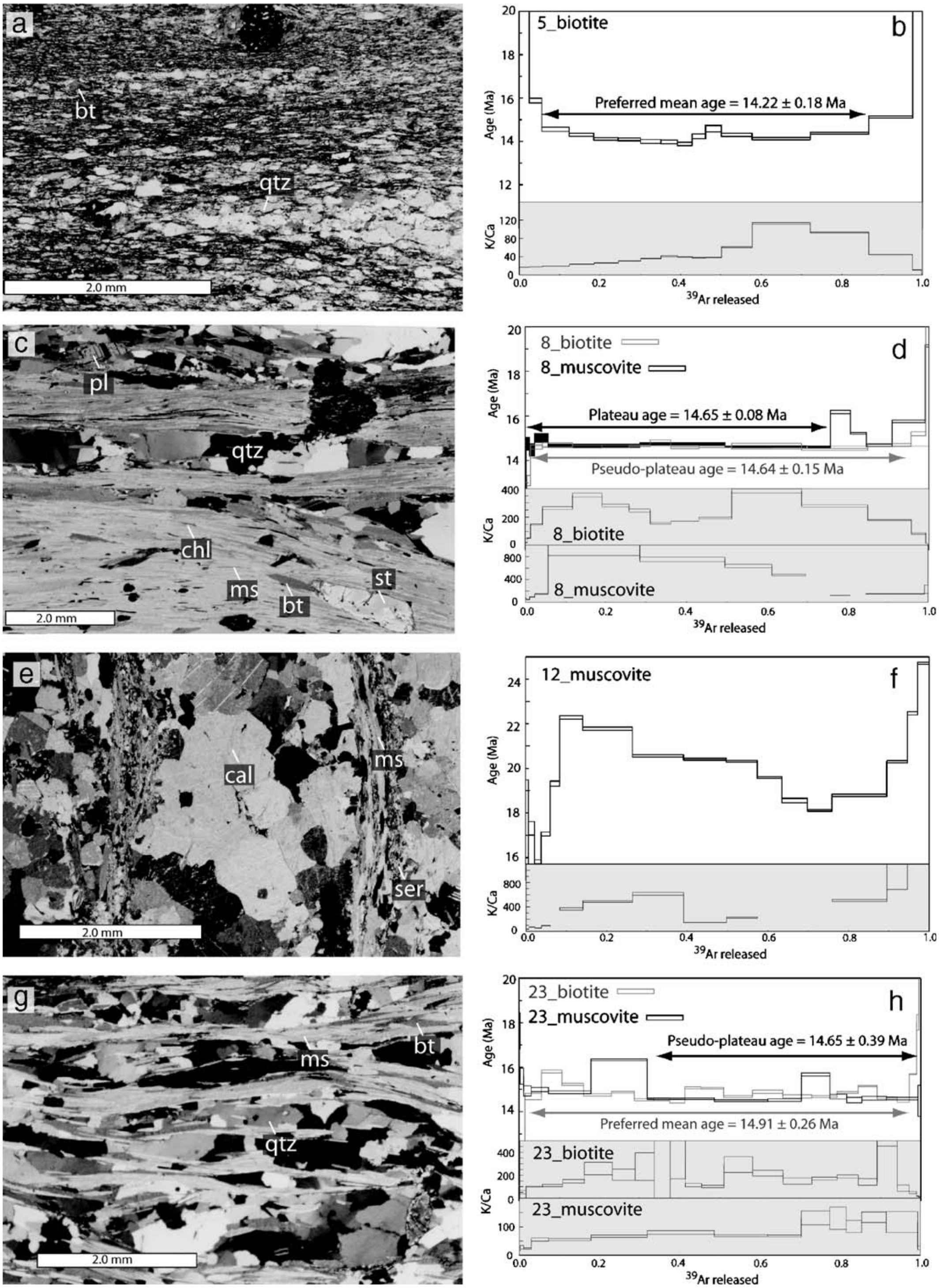

Fig. 5. Photomicrographs and associated biotite and muscovite age spectra. Mineral abbreviations biotite (bt), muscovite (ms), quartz (qtz), garnet (grt), chlorite (chl), sericite (ser), calcite (cal), staurolite (st), plagioclase (pl). Rock and spectra descriptions in text and Table 2.

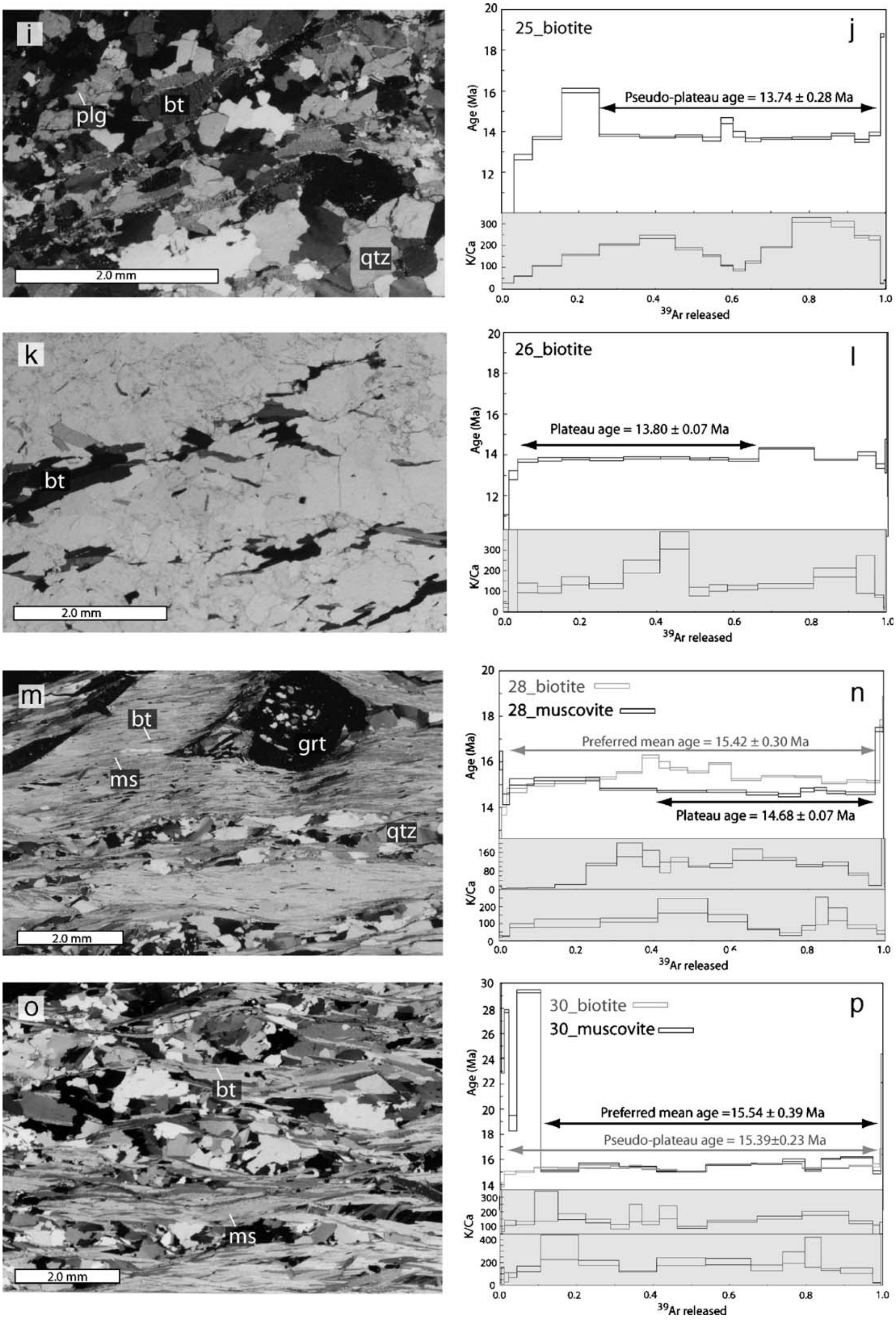

Fig. 5 (*continued*).

markedly relative to the hump-shaped spectra commonly associated with chloritization (Di Vincenzo et al., 2003; see also GD 28), suggests that other processes may have exerted more influence on the $^{40}Ar/^{39}Ar$ spectrum.

In thin section, GD 05 biotites are folded and have strong undulatory extinction, indicating that deformation of the micas occurred at temperatures below mica recrystallization. Deformation may introduce sub-structure into the minerals and thus influence argon diffusivity and retentivity (Kramar et al., 2001; Mulch et al., 2002; Forster and Lister, 2004). We suggest that lower temperature deformation of these biotites generated an intracrystalline structure particularly susceptible to radiogenic argon loss during cooling, resulting in anomalously young ages over much of the sample.

5.4.2. GD 08

The biotite age spectrum for GD 08 (Fig. 5 c,d) is principally composed of concordant steps and yields a well-defined pseudo-plateau age of 14.65±0.08 Ma. Despite general concordancy throughout the biotite spectrum, we were unable to obtain a plateau age because of a discordant step at 815 °C. The muscovite age spectrum (Fig. 5 c,d) is also composed of concordant steps and yields a nearly identical plateau age of ~14.64±0.15 Ma. The concordant spectra and nearly identical cooling ages of coexisting biotite and muscovite in this sample, together with the similar petrographic characteristics and grain size of both micas (Table 2), suggest either that both micas cooled through the same closure temperature or cooled rapidly through different closure temperatures.

5.4.3. GD 12

The GD 12 white mica spectrum (Fig. 5f) is complex, yielding a series of discordant steps ranging in age from 15.8 to 24.7 Ma. The edges of many mica grains in this sample are serrated and contain inclusion-riddled mats of fine-grained sericite (Fig. 5e) indicating localized alteration. The significance of this apparently old age is uncertain given the potential for excess and/or redistributed argon and mica alteration. Similar mica spectra from other Himalayan micas were interpreted to result from inherited excess argon (low temperature steps with anomalously old ages; Maluski et al., 1988) and recoil-induced $^{39}Ar_K$ loss and/or redistribution near grain boundaries (low temperature steps, young ages). We therefore place little emphasis on this result in subsequent discussions.

5.4.4. GD 23

The muscovite spectrum for GD 23 (Fig. 5h) is characterized by two large, anomalous steps at 815 °C and 920 °C which disrupt generally concordant ages over the bulk of the remaining steps and prohibit delineation of a plateau. A pseudo-plateau age of 14.65±0.39 Ma was obtained from concordant steps from 840 °C to 1350 °C, including the 920 °C outlier. Co-existing biotite yields a series of mildly discordant steps from which neither a plateau age nor pseudo-plateau age could be determined. We obtained a preferred mean age of 14.91±0.26 Ma from steps encompassing roughly 96% of the total ^{39}Ar released.

The anomalous steps for GD 23 muscovite are interpreted to indicate either degassing of fluid inclusions containing inherited argon or recoil loss of $^{39}Ar_K$ from interlayers of fine-grained sericite. Fluid inclusions may have been contained within sub-microscopic interlayers of sericite or chlorite, which could account for lower temperature degassing, or within the muscovite grains, which could explain higher temperature degassing.

The general discordance of the GD 23 biotite spectrum is suggestive of sub-microscopic chloritization and consequent $^{39}Ar_K$ recoil-induced redistribution processes (Fergusson and Phillips, 2001; Di Vincenzo et al., 2003) as opposed to fluid inclusion argon release at specific temperature intervals.

5.4.5. GD 25

The GD 25 biotite spectrum (Fig. 5j) contains anomalously young and old ages at low temperature steps followed by a relatively concordant section between temperatures of 700 °C to 1070 °C. The concordant portion contains an anomalous step at 800 °C which prohibits determination of a plateau age. We estimated a pseudo-plateau age of 13.74±0.28 Ma from the concordant section of the spectrum.

The anomalously young ages associated with low temperature steps (≤600 °C) are probably related to $^{39}Ar_K$ redistribution by recoil (Lo et al., 2000). Most of the biotites from this sample suite, with the important exception of GD 05, yield young ages at steps ≤600 °C and therefore appear to have been effected by $^{39}Ar_K$ recoil. Similarly, the relatively old age may have resulted from either recoil-related $^{39}Ar_K$ loss or fluid inclusion degassing. The anomalous step at 800 °C again suggests degassing of $^{39}Ar_K$ depleted chlorite interlayers, despite an absence of visible chlorite in the mineral separate.

5.4.6. GD 26

GD 26 biotite yields a flat age spectrum and well-defined plateau age of 13.80±0.07 Ma between 650–900 °C temperature steps (Fig. 5l). Two anomalously old steps occur at temperatures of 940 °C and 1020 °C. These steps are interpreted to reflect release of inherited argon from fluid inclusions during muscovite breakdown and melting, as inferred for high temperature steps in GD 08 and GD 23 muscovites.

5.4.7. GD 28

GD 28 biotite yields a hump-shaped disturbed spectrum composed of discordant steps ranging in age from ∼13.8 to 15.9 Ma flanked by younger ≤600 °C temperature steps and older ≥1170 °C steps (Fig. 5n).

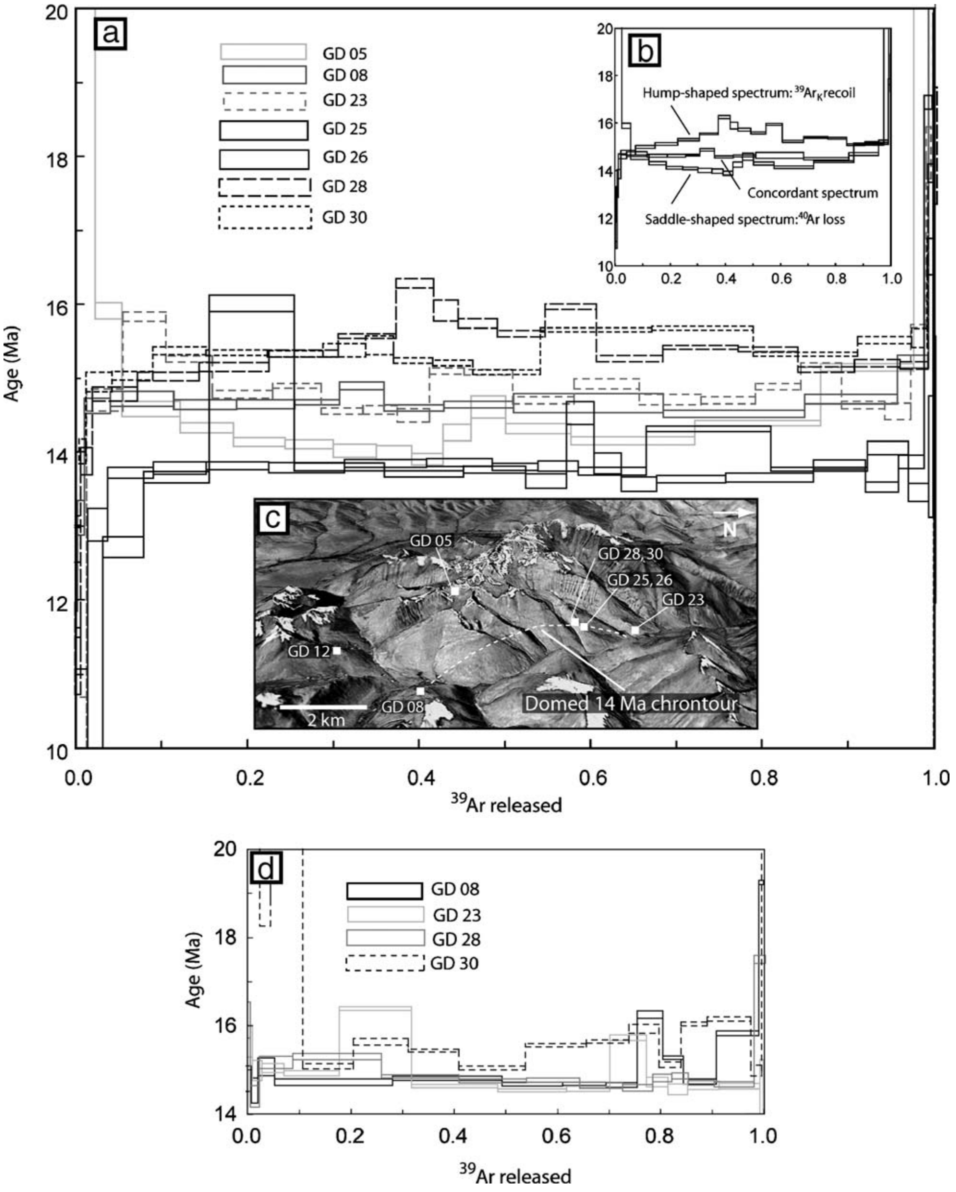

Fig. 6. Compilations of mica age spectra. (a) Compiled biotite age spectra for all samples, showing relationship between ∼13.8 Ma orthogniess ages, followed by a clustering of older ages of ∼14.6 Ma and older from the overlying metasedimentary sequence. (b) Effect of ^{39}Ar$_K$ induced recoil into chlorite interlayers demonstrated by hump shaped spectrum (GD 28) and effect of ^{40}Ar redistribution demonstrated by saddle-shaped spectrum (GD 05). The disturbed spectra are interpreted to reflect petrologically induced departures from well-defined concordant behavior, as demonstrated from GD 08 spectra. We infer that the concordant spectra reflect the true cooling age of the disturbed spectra. (c) Thermochronology sample locations plotted on ASTER image draped over regional DEM, looking west. Lower elevation and older cooling age of GD 23 relative to GD 25, 26 implies a N-dipping 14 Ma chrontour. Similar elevation and older cooling age of GD 08 relative to GD 25, 26 implies that the 14 Ma chrontour must be domed. (d) Compiled muscovite spectra.

Similarly shaped spectra have been attributed to $^{39}Ar_K$ recoil redistribution and differential release of argon from submicroscopic chlorite interlayers (Di Vincenzo et al., 2003). Although chlorite was observed at biotite grain boundaries in thin-section, visibly chloritized biotite grains were identified and discluded from separates during handpicking. We thus infer that submicroscopic chlorite interlayering may have led to older apparent cooling ages at intermediate temperature steps in this sample. Because we derived our preferred mean age of 15.42±0.30 Ma from all discordant steps between 650 and 1110 °C, including the anomalous intermediate temperature steps, we tentatively suggest that this age is too old.

GD 28 muscovite yields concordant age spectrum and a plateau age of 14.68±0.07 Ma for steps between 815 and 1130 °C. Low temperature discordant ages are inferred to reflect $^{39}Ar_K$ recoil-induced redistribution. The muscovite plateau age is younger than the preferred mean age determined from co-existing biotite, consistent with either non-systematic biotite behavior due to chlorite interlayering or biotite closure at temperatures higher than muscovite closure temperatures.

5.4.8. GD 30

Biotite and muscovite spectra from GD 30 yield mildly discordant age steps from which plateau ages could not be obtained (Fig. 5p). A pseudo-plateau age of 15.39±0.23 Ma was obtained from GD 30 biotite and a preferred mean age of 15.54±0.39 Ma was obtained from GD 30 muscovite. The close overlap of spectral patterns and inferred cooling ages suggests either similar mica closure temperatures or rapid mica cooling through different closure temperatures (Fig. 6c). Both the biotite and muscovite spectrum show mild discordancy from low to high temperature steps, inferred to reflect $^{39}Ar_K$ recoil and redistribution. At temperatures ≤ 775 °C, anomalously old muscovite ages may reflect either excess argon (Kelley, 2002) or recoil. At temperatures > 1020 °C, spectral discordancy may be attributable to fluid inclusions.

6. Discussion

6.1. Summary and interpretation of $^{40}Ar/^{39}Ar$ results

Many of the mica analyses presented here yield $^{40}Ar/^{39}Ar$ spectra with varying degrees of discordance. As a result $^{40}Ar/^{39}Ar$ ages for these samples cannot be interpreted as absolute closure ages without some reservation. Nonetheless, greater clarity into the behavior of Kampa Dome micas can be obtained by reconciling individual argon spectra with petrographic observations, and placing these interpretations into a regional context. $^{40}Ar/^{39}Ar$ spectra for each sample (disregarding GD 12) are combined in Fig. 6.

The structurally lowest samples from the Kampa Granite (GD 25, 26) yield the youngest biotite $^{40}Ar/^{39}Ar$ ages and, with the exception of intervening anomalous steps accounting for <15% of the total ^{39}Ar released, most concordant spectrum. We infer that biotite in the Kampa Granite cooled through ~335±50 °C by ~13.7 Ma.

The pelitic schists immediately overlying the Kampa Granite yield concordant (GD 28 muscovite), discordant hump-shaped (GD 28 biotite) and discordant (GD 28 biotite and GD 30 biotite and muscovite) spectra. The GD 28 muscovite spectrum yields a plateau age that is consistent with plateau and pseudo-plateau mica ages from samples at higher structural levels (GD 08, GD 23) while co-existing biotite yielded an older preferred age. We suspect that the anomalous mid-temperature steps in GD 28 biotite reflect chlorite-induced $^{39}Ar_K$ redistribution by recoil (see also GD 23), which resulted in intermediate temperature steps that are older than the actual cooling age (Di Vincenzo et al., 2003). The presence of interlayered chlorite has been linked to hump-shaped spectra for a variety of samples worldwide (Hess et al., 1987; Lo and Onstott, 1989; Reuter and Dallmeyer, 1989; Ruffet et al., 1991; Wright and Dallmeyer, 1991). An alternative explanation for the older GD 28 biotite age is that the closure temperature for biotite was higher than that for muscovite, resulting in an older cooling age for the former. However, differences in closure temperature alone do not explain the anomalous intermediate-temperature steps in the GD 28 biotite spectra that ultimately resulted in the older age. We therefore deduce that GD 28 cooled through 370±50 °C at 14.68±0.07 Ma.

Both the GD 30 biotite and muscovite spectra are disturbed and yield similar preferred mean and pseudo-plateau ages that are older than the plateau age obtained from GD 28 muscovite. Given the close proximity and absence of any observable structure between these two samples we infer that the ~0.7 Ma age difference between GD 28 muscovite and the GD 30 micas reflects either heterogeneous geologic / petrologic features (excess argon, fluid inclusions) or differing amounts of $^{39}Ar_K$ recoil and redistribution. We do not interpret the GD 30 spectra to provide an absolute constraint on the timing of mica cooling throughout this part of the section because samples located immediately above (GD 28 muscovite) and below (GD 25, 26) this sample yield younger cooling ages from more concordant spectra.

At slightly shallower crustal levels within lithologically similar high grade pelitic schist (GD 08), biotite and muscovite spectra yield near-identical, well defined pseudo-plateau and plateau ages of ~14.6 Ma, consistent with the plateau age from GD 28 muscovite. The GD 08 spectra do not appear to be affected by $^{39}Ar_K$ recoil, perhaps because the chlorite in this sample is coarser grained than in the underlying samples, and was recognized and separated from biotite during hand-picking. Given the high degree of concordance within this sample, we are confident that the 14.6 Ma ages accurately reflect the timing of mica cooling. At intermediate crustal levels (GD 23), muscovite "pseudo-plateau" cooling ages also indicate cooling through ~370±50 °C at ~14.6 Ma. Co-existing biotite yields a disturbed spectrum and older apparent age that is interpreted to reflect similar processes that affected the GD 30 and GD 28 biotite spectra.

At the structurally shallowest crustal levels, GD 05 yields a discordant, saddle-shaped age spectrum. A preferred mean age of ~14.2 Ma was derived from intermediate temperature steps. The shape of this spectrum is unique from all other spectra analyzed (Fig. 6b). GD 05 may have been affected by $^{39}Ar_K$ recoil, however, biotite microtextural features unique to this sample, including serrated grain boundaries and intracrystalline deformation, suggest alternative mechanisms are required to explain the spectral discordance. Mineral and fluid inclusions may contain excess argon (Rama et al., 1965) and consequently alter $^{40}Ar/^{39}Ar$ release spectra (Kelley et al., 1986). Although considerable care was taken to exclude micas with any visible mineral inclusions, we cannot absolutely state that inclusions did not play some role in generating anomalous steps in the GD 05 $^{40}Ar/^{39}Ar$ spectrum (and possibly other spectra), either via incorporation of additional K-bearing mineral phases or through release of excess argon trapped in fluid inclusions (Rama et al., 1965; Esser et al., 1997; Kelley, 2002). Sub-solidus deformation of GD 05 biotites may have resulted in argon loss/redistribution through microstructurally controlled diffusion pathways (Kramar et al., 2001; Mulch et al., 2002; Forster and Lister, 2004), resulting in anomalously young, discordant age steps. Given the petrographic evidence indicating mica deformation and inclusions (Table 2) we suggest our preferred mean age of 14.22±0.18 Ma derived from the saddle portion of the spectrum is too young. We are unable to provide an absolute temporal constraint on cooling from GD 05, however we suspect that the ~14.6 Ma steps (650 °C and 900 °C steps, Table 3) bounding the younger saddles are significant given the signature of ~14.6 Ma cooling from the underlying metasedimentary sequence.

In summary, we infer from our $^{40}Ar/^{39}Ar$ results and sample petrography that the metasedimentary rocks composing the carapace of Kampa Dome cooled synchronously through temperatures between 420 °C (upper closure temperature limit for muscovite) and 285 °C (lower closure temperature limit for biotite) at ~14.6 Ma. The Kampa Granite cooled through temperatures of 285–385 °C by 13.7 Ma. The data provide no evidence for an 'inverted thermal profile', although we cannot dismiss the possibility that such a profile may exist at shallower or deeper crustal levels outside of the studied section. We are unable to quantitatively distinguish whether overlapping muscovite and biotite cooling ages in the metasedimentary sequence (e.g., GD 08) reflect rapid cooling through different closure temperatures or uniform cooling through similar closure temperatures. However, our interpretation that rocks presently separated by ~800 m (Fig. 3) cooled at roughly the same time indicates that cooling must have been rapid. If we consider only the temperature range at which biotite and muscovite closure temperatures overlap (320–385 °C) and infer a present mean surface temperature of ~10 °C, we obtain linear cooling rate estimates of ~21–26 °C m.y.$^{-1}$ for the metasedimentary sequence. Applying the same technique to the Kampa Granite using biotite closure temperatures yields a linear cooling rate of ~21–28 °C m.y.$^{-1}$. These rates are slower, but compatible with estimates of cooling rate from metasedimentary and granitic rocks in the Mabja Dome (~45–60 °C m.y.$^{-1}$; Lee et al., in press). If we assume a relatively high, linear and steady-state geothermal gradient of 30–40 °C km^{-1}, as supported by the evidence for a partial melt zone in the mid-crust of southern Tibet (Nelson et al., 1996), we obtain exhumation rates of ~0.5–0.9 mm yr^{-1} for both the metasedimentary rocks and the Kampa Granite. The rates are similar, although slightly lower than ~1–2 mm yr^{-1} exhumation rate estimates obtained from the Kangmar (Lee et al., 2000) and Mabja–Sakya Domes (Zhang et al., 2004; Lee et al., in press). However the rates at Kangmar and Mabja–Sakya were constrained by other lower temperature chronometers (apatite fission-track and $^{40}Ar/^{39}Ar$ K-feldspar thermochronology) and we therefore suspect that exhumation rates may have varied temporally during evolution of the NHGD (Lee et al., 2000, in press).

6.2. Formation of the Kampa Dome

Thermochronologic and structural data may be combined to constrain the timing and mechanisms responsible for the formation of Kampa Dome. High-temperature foliations (S_1 and S_2) are domed indicating that doming occurred subsequent to D_2. Peak metamorphism and leucogranite intrusion occurred during D_2 and therefore also pre-dated doming. No evidence for post-D_2 magmatism was observed in Kampa Dome implying that the dome did not form as a result of diapirism, although we cannot dismiss the possibility that leucogranite plutons may exist at depth. However, no structures indicative of diapirism, such as radial and tangential lineation patterns or dome-outward shearing in all directions (Schwerdtner et al., 1978; Bateman, 1984; Jelsma et al., 1993) were observed in the dome. In light of field observations, structural data, and regional geochronologic data (Zhang et al., 2004; Lee et al., in press; Quigley et al., in review) we therefore infer that the Kampa Dome was not associated with diapirism and formed after the cessation of regional D_2 deformation at ~14.0 to 14.6 Ma (Lee et al., in press).

D_3 brittle–ductile shear zones and faults indicate top-to-N displacement on the N limb of the dome and top-to-S displacement on the S limb of the dome, implying doming occurred during D_3 (Quigley et al., in review). Microstructures associated with D_3 elements imply deformation occurred at temperatures consistent with mica $^{40}Ar/^{39}Ar$ closure temperatures. This indicates that spatial–temporal patterns in mica cooling ages may be strongly reflective of the doming process. Mica chrontours connecting samples of equivalent cooling age in the Kangmar and Mabja–Sakya Dome are domed, suggesting doming occurred at ~11 Ma and ~13 Ma in these domes, respectively (Lee et al., 2000, in press). Our interpretation that the Kampa metasedimentary sequence cooled synchronously at ~14.6 Ma prohibits the construction of chrontours here. However, providing the discordance in mica cooling ages across the Kampa Shear Zone is geologically meaningful, the presence of younger Kampa Granite cooling ages at elevations above some of the flanking metasedimentary samples (Table 2) suggests that a ~14 Ma chrontour separating these samples is also domed across the core of Kampa Dome (Fig. 6c). We therefore tentatively suggest that doming occurred after ~13.7 Ma in the Kampa Dome, consistent with the interpretation of Lee et al. (2000, in press).

The ‘inverted thermal profile’ revealed by mica thermochronology from the Kangmar and Mabja–Sakya Domes led to the conclusion that doming resulted from S-directed thrusting of mid-crustal rocks over cold Tethyan sediments (Lee et al., 2000, in press). The apparent absence of such a profile in the Kampa Dome neither confirms nor refutes this hypothesis. However, the presence of numerous, brittle–ductile extensional D_3 structures and youngest $^{40}Ar/^{39}Ar$ cooling ages at depth suggests a cooling pattern reflective of extensional exhumation and top–down conduction, as opposed to refrigeration due to cold underthrust rocks at depth. We therefore suspect that upper crustal extension was at least as important as basal thrusting in governing mica cooling patterns and the domal geometry of Kampa Dome.

The ~0.8 m.y. discordance in cooling age across the Kampa Shear Zone may reflect either (1) different mica closure temperatures between the Kampa Granite and metasedimentary schists, and/or (2) ~14.6 Ma to 13.7 Ma reheating and subsequent re-cooling of Kampa Granite biotites without influencing ~14.6 Ma micas in the schists, and/or (3) post 13.7 Ma juxtaposition of rocks with different cooling histories across the Kampa Shear Zone. We are unable to quantitatively assess the first hypothesis but note that micas in the Kangmar Granite are older than those in the overlying schist (Debon et al., 1986; Chen et al., 1990; Lee et al., 2000), opposite to the relationship observed in Kampa Dome. We therefore suspect that this age variation is geologically meaningful and indicative of either localized reheating of the Kampa Granite biotites or structural omission of part of the intervening section. No post-D_2 plutons were observed in Kampa Dome and we are reluctant to suggest that a distant pluton would have reset the granitic biotites without affecting the metasedimentary micas only 20–30 m up-section. We therefore conclude that the pluton-induced reheating of micas at the base of the sequence inferred for the Mabja–Sakya Dome did not generate the pattern observed here (Lee et al., in press). It is possible that syn-D_3 viscous shear-heating in the Kampa Shear Zone may have locally reset Kampa Granite micas without perturbing the metasedimentary sequence. Shear heating has elsewhere been hypothesized to explain thermal patterns and melting along the Main Central Thrust and STDS, albeit on a considerably larger scale (Harrison et al., 1997). However, it is unclear why such a cooling pattern resulting strictly from shear heating along the Kampa Shear Zone would not also be observed adjacent to the Kangmar detachment in Kangmar Dome (Chen et al., 1990), where instead, Kangmar Granite micas are older than micas within the metasedimentary sequence.

An additional explanation for this age difference is that the metasedimentary rocks and Kampa Granite had distinct cooling histories before being juxtaposed along the Kampa Shear Zone (e.g., Chen et al., 1990). Kampa Granite rocks may have been exhumed from deeper crustal levels or laterally translated from areas of higher heat flow subsequent to biotite closure. We favor this hypothesis in light of our evidence for greenschist facies and brittle deformation along the Kampa Shear Zone that is likely to have occurred at temperature below mica closure temperatures.

The Kampa Dome shares several common features with 'typical' extensional metamorphic core complexes (Brun and Van Den Driessche, 1994; Tirel et al., 2004); including (1) the presence of a domed, major detachment zone (Kampa Shear Zone) that places younger metasedimentary rocks on older granitic rocks, (2) the occurrence of high-temperature to low-temperature (brittle) deformation features within this zone, (3) the abundance of normal-sense shear zones and brittle faults that dissect the metasedimentary carapace above this zone, and (4) an apparent discontinuity in $^{40}Ar/^{39}Ar$ mica ages across this zone (Quigley et al., in review). However, unlike typical metamorphic core complexes, the Kampa Dome developed in the middle of a collisional orogen bound by major thrust fault systems to the north (Gandese Thrust, Renbu–Zedong Thrust; Yin et al., 1994; Ratschbacher et al., 1994; Quidelleur et al., 1997) and south (Main Central Thrust; Harrison et al., 1995; Coleman and Parrish, 1995). In addition, the Kampa Dome lies in the hangingwall of the Gyirong–Kangmar Thrust (Fig. 1) (Burg and Chen, 1984) and may be situated directly above an antiformal duplex in the hangingwall of a crustal ramp above the Main Himalayan Thrust (Hauck et al., 1998). Despite these regional observations, no field evidence supporting end-member thrust duplexing, such as flat-lying thrust planes or duplex systems, was observed in Kampa Dome.

We suggest that the Kampa Dome formed as a result of two coeval processes: (1) D_3 crustal thinning and extension in the overlying metasedimentary sequence, which allowed for (2) squeezing and upward insertion of mid-crust into the extending crust during thrusting over a frontal ramp associated with the Gyirong–Kangmar Thrust. It is possible that mid-crustal channel flow aided in exhumation by forcing more material into the base of the rising dome (Beaumont et al., 2004), although no field evidence for syn-doming ductile flow was directly observed. We suspect that extension occurred in response to gravitational collapse of overthickened crust (Royden and Burchfiel, 1987) and therefore correlate the Kampa Shear Zone with the STDS, although the timing at which these structures became disconnected is unknown. Our thermochronologic data provide no clear evidence for an inverted thermal gradient in Kampa Dome, which may indicate that rocks within the dome cooled through mica closure temperatures prior to thrusting along the Gyirong Kangmar Thrust. Differences in mica cooling patterns within the NHGD may reflect along-strike variations in the geometry of the Gyirong Kangmar Thrust and/or variations in the magnitude and intensity of upper crustal extension. Our thermochronologic data suggest cooling occurred in response to tectonic exhumation, possibly coupled with increased surface denudation at the site of the rising dome.

7. Conclusions

The Kampa Dome is cored by Cambrian granite gneiss overlain by a sequence of Paleozoic to Mesozoic sedimentary rocks that were strongly deformed, metamorphosed, and intruded by leucogranites during Himalayan orogenesis. New $^{40}Ar/^{39}Ar$ thermochronology reveals that the Kampa Dome cooled rapidly from ~14.6 Ma to 13.7 Ma in response to top-down conduction related to crustal extension and/or surface denudation. Doming occurred after ~13.7 Ma in response to coeval crustal extension in the metasedimentary sequence, S-vergent thrusting at depth, and erosion. Continued movement along the Kampa Shear Zone during doming may have juxtaposed rocks with different cooling histories. Despite sharing many similarities with adjacent NHGD, the Kampa Dome contains differing amounts of syn-tectonic leucogranite, a prominent shear zone with evidence for high-temperature to brittle deformation, and a mica cooling pattern indicative of top-down, as opposed to bottom-up, conductive cooling. Subtle differences along the strike of the North Himalayan antiform may relate to changes in geometry of the Gyirong Kangmar Thrust and/or differences in the magnitude and intensity of upper crustal extension.

Acknowledgements

We thank J. Lee, B. Hacker, A. Aikman and Tectonophysics editor J.P. Burg for reviews that greatly improved the manuscript. We thank S. Szczepanski for help with argon data reduction, Da Tai for confident cooking of field meals in adverse conditions and the Chinese Academy of Sciences for financial and logistical support.

References

Aoya, M., Wallis, S.R., Terada, K., Lee, J., Kawakami, T., Wang, Y., Heizler, M., 2005. North–south extension in the Tibetan crust triggered by granite emplacement. Geology 33 (11), 853–856.

Aoya, M., Wallis, S.R., Kawakami, T., Lee, J., Wang, Y., in press. The Malashan metamorphic complex in southern Tibet: comparative study with Kangmar Dome with special reference to kinematics of deformation and origin of associated granites. In Law, R.D., Searle, M.P., Godin, L. (Eds.), Geological Society of London Special Publication Channel Flow, Ductile Extrusion and Exhumation of Lower-Mid-Crust in Continental Collision Zones.

Bateman, R., 1984. On the role of diapirism in the segregation, ascent, and final emplacement of granitoid magmas. Tectonophysics 110, 211–231.

Beaumont, C., Jamieson, R.A., Nguyen, M.H., Medvedev, S., 2004. Crustal channel flows: 1. Numerical models with applications to the tectonics of the Himalayan–Tibetan orogen. Journal of Geophysical Research 109, B06406, doi:10.1029/2003JB002809.

Berger, G.W., York, D., 1970. Precision of the ^{40}Ar–^{39}Ar dating technique. Earth and Planetary Science Letters 9, 39–44.

Brookfield, M.E., 1993. The Himalayan passive margin from Precambrian to Cretaceous times. Sedimentary Geology 84, 1–35.

Brun, J.P., Van Den Driessche, J., 1994. Extensional gneiss domes and detachment faults—structure and kinematics. Bulletin de la Société Géologique de France 165, 519–530.

Burchfiel, B.C., Zhiliang, C., Hodges, K.V., Yuping, L., Royden, L.H., Changrong, D., Jiene, X., 1992. The south Tibetan detachment system, Himalayan orogen: extension contemporaneous with and parallel to shortening in a collisional mountain belt. Special Paper-Geological Society of America 269. 41 pp.

Burg, J.P., 1983. Carte géologique du sud du Tibet: Centre Nationale de la Recherche Scientifique, scale 1:500000.

Burg, J.P., Chen, J.M., 1984. Tectonics and structural zonation of southern Tibet, China. Nature 311, 219–223.

Burg, J.P., Guiraud, M., Chen, G.M., Li, G.C., 1984. Himalayan metamorphism and deformations in the North Himalayan Belt (southern Tibet, China). Earth and Planetary Science Letters 69, 391–400.

Chen, Z., Liu, Y., Hodges, K.V., Burchfiel, B.C., Royden, L.H., Deng, C., 1990. The Kangmar Dome: a metamorphic core complex in southern Xizang (Tibet). Science 250, 1552–1556.

Coleman, M.E., Parrish, R.R., 1995. Constraints on Miocene high-temperature deformation and anatexis within the greater Himalaya from U–Pb geochronology. Eos, Transactions-American Geophysical Union 76, F708.

Debon, F., Le Fort, P., Sheppard, S.M.F., Sonet, J., 1986. The four plutonic belts of the Transhimalaya–Himalaya: a chemical, mineralogical, isotopic and chronological synthesis along a Tibet–Nepal section. Journal of Petrology 27, 281–302.

Di Vincenzo, G.D., Viti, C., Rocchi, A., 2003. The effect of chlorite interlayering on ^{40}Ar–^{39}Ar biotite dating: an ^{40}Ar–^{39}Ar laser-probe and TEM investigation of variably chloritised biotites. Contributions to Mineralogy and Petrology 145, 643–658.

Dong, H., Hall, C.M., Halliday, A.N., Peacor, D.R., Merriman, R.J., Roberts, B., 1997. ^{40}Ar/^{39}Ar illite dating of Late Caledonian (Acadian) metamorphism and cooling of K-bentonites and slates from the Welsh Basin, UK. Earth and Planetary Science Letters 150, 337–351.

Eskola, P.E., 1949. The problem of mantled gneiss domes. Quarterly Journal of the Geological Society of London 104, 461–476.

Esser, R.P., McIntosh, W.C., Heizler, M.T., Kyle, P.R., 1997. Excess argon in melt inclusions in zero-age anorthoclase feldspar from Mt Erebus, Antarctica, as revealed by the ^{40}Ar/^{39}Ar method. Geochimica et Cosmochimica Acta 61, 3789–3801.

Fergusson, C.L., Phillips, D., 2001. ^{40}Ar/^{39}Ar and K–Ar age constraints on the timing of regional deformation, south coast of New South Wales, Lachlan Fold Belt: problems and implications. Australian Journal of Earth Sciences 48, 395–408.

Forster, M.A., Lister, G.S., 2004. The interpretation of ^{40}Ar/^{39}Ar apparent age spectra produced by mixing: application of the method of asymptotes and limits. Journal of Structural Geology 26, 287–305.

Gaetani, M., Garzanti, E., 1991. Multicyclic history of the northern India continental margin (northwestern Himalaya). American Association of Petroleum Geologists Bulletin 75, 1427–1446.

Gansser, A., 1964. Geology of the Himalayas. Wiley-Interscience, London.

Grove, M., 1993. Thermal histories of southern California basement terrains. PhD dissertation, University of California, Los Angeles.

Grove, M., Harrison, T.M., 1996. ^{40}Ar diffusion in Fe-rich biotite. American Mineralogist 81, 940–951.

Hames, W.E., Bowring, S.A., 1994. An empirical evaluation of the argon diffusion geometry in muscovite. Earth and Planetary Science Letters 124, 161–167.

Harrison, T.M., McDougall, I., 1981. Excess ^{40}Ar in metamorphic rocks from Broken Hill, New South Wales: implications for ^{40}Ar/^{39}Ar age spectra and the thermal history of the region. Earth and Planetary Science Letters 55, 123–149.

Harrison, T.M., Duncan, I., McDougall, I., 1985. Diffusion of ^{40}Ar in biotite: temperature, pressure and compositional effects. Geochimica et Cosmochimica Acta 49, 2461–2468.

Harrison, T.M., Copeland, P., Kidd, W.S.F., Lovera, O.M., 1995. Activation of the Nyainqentanghla shear zone: implications for uplift of the southern Tibetan Plateau. Tectonics 14, 658–676.

Harrison, T.M., Lovera, O.M., Grove, M., 1997. New insights into the origin of two contrasting Himalayan granite belts. Geology 25 (10), 899–902.

Hauck, M.L., Nelson, K.D., Brown, L.D., Zhao, W., Ross, A.R., 1998. Crustal structure of the Himalayan orogen at approximately 90° east longitude from Project INDEPTH deep reflection profiles. Tectonics 17, 481–500.

Hess, J.C., Lippolt, H.J., Wirth, R., 1987. Interpretation of ^{40}Ar/^{39}Ar spectra of biotites: evidence from hydrothermal degassing experiments and TEM studies. Chemical Geology. Isotope Geoscience 66, 137–149.

Hess, J.C., Lippolt, H.J., Gurbanov, A.G., Michalski, I., 1993. The cooling history of the Late Pliocene Eldzhurtinskiy granite (Caucasus, Russia) and the thermochronological potential of grain-size/age relationships. Earth and Planetary Science Letters 117, 393–406.

Hodges, K.V., 2000. Tectonics of the Himalayan and southern Tibet. Geological Society of America Bulletin 112, 324–350.

Jelsma, H.A., Van Der Beek, P.A., Vinyu, M.L., 1993. Tectonic evolution of the Bindura–Shamva greenstone belt (northern Zimbabwe): progressive deformation around diapiric batholiths. Journal of Structural Geology 15, 163–176.

Kelley, S.P., 1988. The relationship between K–Ar mineral ages, mica grain sizes and movement on the Moine Thrust Zone, NW Highlands, Scotland. Journal of the Geological Society (London) 145, 1–10.

Kelley, S., 2002. Excess argon in K–Ar and Ar–Ar geochronology. Chemical Geology 188, 1–22.

Kelley, S., Turner, S., Butterfield, A.W., Shepard, T.J., 1986. The source and significance of argon in fluid inclusions from areas of mineralization. Earth and Planetary Science Letters 79, 303–318.

Kramar, N., Cosca, M.A., Hunziker, J.C., 2001. Heterogenous ^{40}Ar* distributions in naturally deformed muscovite: in situ UV-laser ablation evidence for microstructurally controlled intragrain diffusion. Earth and Planetary Science Letters 192, 377–388.

Lee, J., Dinklage, W.S., Hacker, B.R., Wang, Y., Gans, P.B., Calvert, A., Wan, J., Chen, W., Blythe, A., McClelland, W., 2000. Evolution of the Kangmar Dome, southern Tibet: structural, petrologic, and thermochronologic constraints. Tectonics 19, 872–896.

Lee, J., Hacker, B., Wang, Y., 2004. Evolution of North Himalayan gneiss domes: structural and metamorphic studies in Mabja Dome, southern Tibet. Journal of Structural Geology 204, 2297–2316.

Lee, J., McClelland, W., Wang, Y., Blythe, A., McWilliams, M., in press. Oligocene–Miocene middle crustal flow in southern Tibet: geochronologic studies in Mabja Dome. In: Law, R.D., Searle, M. P., Godin, L. (Eds.), Geological Society of London Special Publication Channel Flow, Ductile Extrusion and Exhumation of Lower-Mid-Crust in Continental Collision Zones.

Le Fort, P., 1975. Himalayas: the collided range. Present knowledge of the continental arc. American Journal of Science 275, 1–44.

Le Fort, P., 1986. Metamorphism and magmatism during the Himalayan. In: Coward, M.P., Reis, A.C. (Eds.), Collission Tectonics. Geological Society, London, Special Publications, vol. 19, pp. 159–172.

Le Fort, P., Cuney, M., Deniel, C., France-Lanord, C., Sheppard, S.M.F., Upreti, B.N., Vidal, P., 1987. Crustal generation of the Himalayan leucogranites. Tectonophysics 134, 39–57.

Lister, G.S., Baldwin, S.L., 1996. Modelling the effect of arbitrary *P*–*T*–*t* histories on argon diffusion in minerals using the MacArgon program for the Apple Macintosh. Tectonophysics 253, 83–109.

Lo, C.H., Onstott, T.C., 1989. ^{39}Ar recoil artefacts in chloritized biotite. Geochimica et Cosmochimica Acta 53, 2697–2711.

Lo, C.H., Lee, J.K., Onstott, T.C., 2000. Argon release mechanisms of biotite in vacuo and the role of short-circuit diffusion and recoil. Chemical Geology 165, 135–166.

Maluski, H., Matte, P., Brunel, M., 1988. Argon 39–Argon 40 dating of metamorphic and plutonic events in the north and high Himalayas belts (southern Tibet–China). Tectonics 7, 299–326.

Markley, M., Teyssier, C., Cosca, M., 2002. The relation between grain size and ^{40}Ar/^{39}Ar date for Alpine white mica from the Siviez–Mischabel Nappe, Switzerland. Journal of Structural Geology 24, 1937–1955.

McDougall, I., Harrison, T.M., 1999. Geochronology and thermochronology by the ^{40}Ar/^{39}Ar method. Oxford University Press, New York. 212 pp.

Mulch, A., Cosca, M.A., Handy, M.R., 2002. In situ UV-laser ^{40}Ar/^{39}Ar geochronology of a micaceous mylonite: an example of defect-enhanced argon loss. Contributions to Mineralogy and Petrology 142, 738–752.

Nelson, K.D., Zhao, W., Brown, L.D., Kuo, J., Che, J., Liu, X., Klemperer, S.L., Makovsky, Y., Meissner, R., Mechie, J., Kind, R., Wenzel, F., Ni, J., Nabelek, J., Chen, L., Tan, H., Wei, W., Jones, A.G., Booker, J., Unsworth, M., Kidd, W.S.F., Hauck, M., Alsdorf, D., Ross, A., Cogan, M., Wu, C., Sandvol, E.A., Edwards, M., 1996. Partially molten middle crust beneath southern Tibet: synthesis of project INDEPTH results. Science 274, 1684–1688.

Pickles, C.S., Kelley, S.P., Reddy, S.M., Wheeler, J., 1997. Determination of high spatial resolution argon isotope variations in metamorphic biotites. Geochimica et Cosmochimica Acta 61 (18), 3809–3883.

Quidelleur, X., Grove, M., Lovera, O.M., Harrison, T.M., Yin, A., Ryerson, F.J., 1997. The thermal evolution and slip history of the Renbu Zedong thrust, southeastern Tibet. Journal of Geophysical Research 102, 2659–2679.

Quigley, M.C., 2006. Continental tectonics and landscape evolution in south-central Australia and southern Tibet. Unpublished PhD thesis, The University of Melbourne. 220 pp.

Quigley, M.C., Liangjun, Y., Xiaohan, L., Wilson, C.J.L., Sandiford, M., 2004. Genesis and evolution of the Kampa Dome: insights into the middle and upper crustal deformation of southern Tibet: Lhasa, China. 4th International Symposium on the Tibetan Plateau, Programs and Abstracts, vol. 48.

Quigley, M.C., Liangjun, Y., Gregory, C., Corvino, A., Wilson, C., Sandiford, M., Xiaohan, L., Lister, G., in review. Origin and evolution of North Himalayan middle crust, Kampa Dome, southern Tibet, Tectonophysics.

Rama, S.N., Hart, S.R., Roedder, E., 1965. Excess radiogenic argon in fluid inclusions. Journal of Geophysical Research 70, 509–511.

Ratschbacher, L., Frisch, W., Liu, G., Chen, C., 1994. Distributed deformation in southern and western Tibet during and after the India–Asia collision. Journal of Geophysical Research 99, 19,917–19,945.

Renne, P., Swisher, C., Deino, A., Karner, D., Owens, T., DePaolo, D., 1998. Intercalabration of standards, absolute ages and uncertainties in ^{40}Ar/^{39}Ar dating. Chemical Geology 145, 117–152.

Reuter, A., Dallmeyer, R.D., 1989. K–Ar and ^{40}Ar/^{39}Ar dating of cleavage formed during very low-grade metamorphism: a review. In: Daly, J.S., Cliff, R.A., Yardley, B.W.D. (Eds.), Evolution of Metamorphic Belts. Special Publication-Geological Society of London, vol. 43, pp. 161–171.

Royden, L.H., Burchfiel, B.C., 1987. Thin-skinned north–south extension within convergent Himalayan region: gravitational collapse of a Miocene topographic front. In: Coward, M.P., Dewey, J.F., Hancock, P.L. (Eds.), Continental Extensional Tectonics, Geological Society Special Publication, vol. 28, pp. 611–619.

Ruffet, G., Féraud, G., Amouric, M., 1991. Comparison of ^{40}Ar–^{39}Ar conventional and laser dating of biotites from the north Trégor Batholith. Geochimica et Cosmochimica Acta 55, 1675–1688.

Scharer, U., Xu, R., Allegre, C., 1986. U–(Th)–Pb systematics and ages of Himalayan leucogranites, south Tibet. Earth and Planetary Science Letters 77, 35–48.

Schwerdtner, W.M., Sutcliff, R.H., Troeng, B., 1978. Patterns of total strain in the crustal region of immature diapirs. Canadian Journal of Earth Sciences 15, 1437–1447.

Steiger, R.J., Jäger, E., 1977. Subcommission on geochronology: convention on the use of decay constants in geo- and cosmochronology. Earth and Planetary Science Letters 36, 359–362.

Tapponnier, P., Peltzer, G., Le Dain, A.Y., Armijo, R., Cobbold, P., 1982. Propagating extrusion tectonics in Asia: new insights from simple experiments from plasticine. Geology 10, 611–615.

Tirel, C., Brun, J.-P., Burov, E., 2004. Dome structures in collisional orogens: mechanical investigation of the gravity/compression interplay. In: Whitney, D.L., Teyssier, C., Siddoway, C.S (Eds.), Gneiss Domes and Orogeny. Geological Society of America Special Paper, vol. 380, pp. 47–66.

Watts, D.R., Harris, N., 2002 NASA GLENN SOARS Working Group, 2005. Mapping granite and gneiss in domes along the North Himalayan antiform with ASTER SWIR band ratios. GSA Bulletin 117 (7–8), 879–886, doi:10.1130/B25592.1.

Whitney, D.L., Teyssier, C., Vanderhaeghe, O., 2004. Gneiss domes and crustal flow. In: Whitney, D.L., Teyssier, C., Siddoway, C.S. (Eds.), Gneiss Domes and Orogeny. Geological Society of America Special Paper, vol. 380, pp. 15–33.

Willems, H., Zhou, Z., Zhang, B., Graefe, K.U., 1996. Stratigraphy of the Upper Cretaceous and Lower Tertiary strata in the Tethyan

Himalayas of Tibet (Tingri area, China). Geologische Rundschau 85, 723–754.

Wright, T.O., Dallmeyer, R.D., 1991. The age of cleavage development in the Ross orogen, northern Victoria Land, Antarctica: evidence from $^{40}Ar/^{39}Ar$ whole-rock slate ages. Journal of Structural Geology 13, 677–690.

Yin, J., Xu, J., Liu, C., Li, H., 1988. The Tibetan Plateau: regional stratigraphic context and previous work. In: Chang, C., Shackleton, R., Dewey, M., Yin, F. (Eds.), The Geological Evolution of Tibet: Royal Society of London Philosophical Transactions, vol. 327, pp. 379–413.

Yin, A., Harrison, T.M., Ryerson, F.J., Chen, W., Kidd, W.S.F., Copeland, P., 1994. Tertiary structural evolution of the Gangdese thrust system, southeastern Tibet. Journal of Geophysical Research 99, 18175–18201.

York, D., Lopez Martinez, M., 1986. The two-faced mica. Geophysical Research Letters 9, 973–975.

Zengqian, L., Shupei, J., Yifu, Z., Shaoxian, Y., Changxing, A., Younian, Z., Yaomin, L., Huaida, W., Jian'e, X., Jinqing, H., Tieying, G., 1986. Geological map of Qinghai–Xizang (Tibet) Plateau and adjacent area. Chengdu Institute of Geological Sciences, Chinese Academy of Sciences, scale 1:150,000, 6 sheets.

Zhang, Q., Zhou, Y., Li, D., Wu, H., 1986. Principal features of the gneissic dome and its peripheral metamorphic zones in Kangma of Xizang, China. Scientia Geologica Sinica 2, 125–133.

Zhang, H., Harris, N., Parrish, R., Kelley, S., Li, Z., Rogers, N., Argles, T., King, J., 2004. Causes and consequences of protracted melting of the mid-crust exposed in the North Himalayan antiform. Earth and Planetary Science Letters 228, 195–212.